AIAA 2010-3863

# Experimental and numerical investigation of the flow-induced resonance of slender deep cavities that resemble automotive door gaps

A.T. de Jong* and H. Bijl †



**Cavity aeroacoustic noise is relevant for aerospace and automotive industries and widely investigated since the 1950's. Most investigations so far consider cavities where opening length and width are of similar scale. The present investigation focuses on a less investigated setup, namely cavities that resemble the door gaps of automobiles. These cavities are both slender (width much greater than length or depth) and partially covered. Furthermore they are under influence of a low Mach number flow with a relatively thick boundary layer. Under certain conditions, these gaps can resonate with the flow.**

**The present investigation attempts to reveal the aeroacoustic mechanism of this tonal noise. Also the ability to simulate the resonance behavior using the Lattice Boltzmann method (LBM) is evaluated**

**Experiments have been conducted on simplified geometries, where hotwire, high speed PIV and microphone measurements have been used. The opening geometry and boundary layer properties have been varied. Using the PIV results, the observed influences of the opening geometry on base mode resonance are explained.**

**With increasing velocity, several resonance modes occur. In order to obtain higher mode shapes, the cavity acoustic response is simulated using LBM and compared with experiment. Using the frequency-filtered simulation pressure field, the higher modes shapes are retrieved. Based on this an analytical model is derived that shows good agreement with the simulations and experimental results.**

**LBM based flow simulations show that the turbulent fluctuation content of the boundary layer is important to correctly simulate the flow induced resonance response. When unsteady fluctuations are implemented in the inlet of the simulation, the cavity excitation shows good resemblance with experiment.**

## I. Introduction

Noise reduction is an important part of engineering design in the transportation industries. Airplanes, automobiles and trains all produce noise that disturbs passengers, operators and the surrounding communities. On a typical car geometry there are several possible sources for aeroacoustic sound production. These include broadband wind noise due to turbulence, whistling of spoilers and antennas, sunroof buffeting and flow induced resonance of the trunk lid and door gaps.

From a physical point of view the aeroacoustic mechanism of door gap resonance is not entirely clear. These structures are slender (width much higher than length or depth), covered and under influence of a thick boundary layer. Most of the focus in research in the past has been put on other cavity geometries. For example, in the aircraft industry, most focus has been put on open shallow cavities. These cavities resemble aircraft weapon bays and landing gear wheel wells.[1] Deep cavity resonance has also been a topic of interest, for example in side branches of pipe systems.[2,3] Covered cavity geometries have been investigated in detail, where the cavity often behaves like a Helmholtz resonator. For example Dequand et. al.[4,5] investigated the resonance lock-on amplitude of several rectangular Helmholtz resonator geometries under a thin boundary

*PhD candidate, Delft University of Technology, Department of Aerodynamics, Faculty of Aerospace Engineering, Kluyverweg 2, Delft, the Netherlands

†Professor, Delft University of Technology, Department of Aerodynamics, Faculty of Aerospace Engineering, Kluyverweg 2, Delft, the Netherlands

layer flow. Examples of applications are the sound generation in flute like instruments,[6–8] the buffeting of open car sunroofs and side windows[9,10] and Helmholtz resonators used in acoustic liners.[11]

The current investigation concerns a special setup relevant in the automobile industry, the tonal noise from automobile gaps. These covered cavities are slender (width much larger than length or depth) and under influence of a low Mach number flow ($M \approx 0.1$) with a relatively thick boundary layer. Both slenderness and a thick boundary layer reduce the resonance response of a cavity. Howe's theory[12] indicated that an increased aspect ratio modifies the impedance, thereby reducing resonance. Kooijman et. al.[13] showed that by increasing the boundary layer momentum thickness compared to the opening length, the instability of the opening shear layer is reduced. In fact, in general door gaps only show a passive response to the flow, although there are cases where a resonance lock-on can occur.

Door gap structures have not been examined in great detail, although quite some investigations on geometries of this kind can be found in literature. For example Nelson[14,15] experimentally analyzed a Helmholtz resonator with laser Doppler velocimetry, where an opening slot of 600 by 10 mm was excited by a grazing flow of 16 to 27 m/s. In addition, Henderson[16,17] presented benchmark experimental data of a resonator with a 460 by 8 mm slot with a thick boundary layer flow of 45 to 60 m/s. Mongeau et. al.[18] show experimental results of a 25 cm wide cavity that resembles a door gap, including a seal fixture, where the cavity showed a passive response to the outside flow.

The current investigation is set up to investigate cavity acoustic resonance behavior in order to reveal the influence of gap geometry and flow conditions on resonance. For shallow cavities, it is known that the boundary layer has a large influence on the resonance behavior, however this has never been quantified in detail for door gap like structures. For side-branches in pipe systems, the influence of the upstream and downstream opening edges can be considerable. Therefore it is expected to have a large influence on gap resonance behavior as well. Different upstream and downstream edge round-offs are implemented. Furthermore in the currently investigated covered cavity, the overhang location can be moved between the upstream and downstream edges. Also the boundary layer thickness is varied.

Special focus is put on resonances with spanwise variations due to the slender dimensions. Spanwise modes have been identified in shallow cavities in a large eddy simulation of a weapon bay by Larchevêque,[19] corresponding to simple spanwise room modes. For covered cavities, Henderson mentioned the possible existence of modes with spanwise variation. But the pressure excitations were measured at a single spanwise location and it was therefore not possible to identify these modes. Mongeau observed passive low amplitude spanwise modes which were not coupled to higher amplitude excitations. Therefore they do not correspond to spanwise varying resonance modes observed in the current research.

Three dimensional acoustic and flow simulations are performed using the Lattice Boltzmann method (LBM) and compared with experimental results. LBM is a method using kinetic theory to simulate compressible flows at low Mach numbers. Special attention is put on the effect of inflow conditions on cavity resonance.

The present numerical and experimental investigation attempts to reveal and describe the flow induced resonance properties of simplified door gap geometries in detail. The investigation is also performed to reveal whether, and under what conditions the aeroacoustic resonance can be simulated correctly. Section II summarizes the theory of gap noise resonance. Both windtunnel results and Lattice Boltzmann Method based flow simulations are used in the investigation. Sections III and IV explain the used experimental and numerical setups. The experimental results are given in section V. The influence of geometry and flow parameters for the base resonance modes is presented in section VI. The higher modes with spanwise variation are investigated in section VII. Finally the CFD simulations of the cavity geometry are presented in section VIII.

## II. Theory: Cavity resonance modes

This section briefly explains the possible aeroacoustic mechanisms for the investigated setups. A cavity volume can act as an acoustic resonator to an excitation source in the cavity neck region.

The excitation can either be due to a feedback mechanism of the perturbed shear layer or due to passive excitation by the pressure fluctuations in the turbulent flow[20] (turbulent rumble). In case of feedback, the shear layer can roll up into discrete vortices impinging on the opening downstream edge coherently (a Rossiter mode),[1] or exhibit a flapping shear layer motion. In the low Mach number limit, a feedback mode corresponds to excitation at a fixed Strouhal number $Sr = \frac{f\delta}{U_\infty}$, with $f$ the frequency, $\delta$ the slot opening

length and $U_\infty$ the free stream velocity. If the excitation frequency is close to a resonance frequency, lock-on can occur and the system can resonate. In case of turbulent rumble the resonance should effectively be independent of velocity.

The resonance method can either be of a Helmholtz type or of a standing wave type. In Helmholtz-like resonance the mass of air in the cavity is coherently compressed and expanded. The equation for a Helmholtz resonator is:[21]

$$f_H = \frac{c}{2\pi}\sqrt{\frac{S}{VH'}}. \tag{1}$$

Here $V$ is the cavity volume, $S$ is the cavity neck surface area and $H'$ is the corrected vertical length of the cavity neck. The relation between the real vertical cavity neck height $H$ and $H'$ is $H' = H + h$, where $h$ is an end correction factor to account for the added resonating mass above and below the opening. For non-slender openings it is based on the surface area $h \propto \sqrt{S}$, whereas in the slotted opening of the current investigation, it is assumed to be related to the opening length only $h \propto \delta$ and independent of the slot width $W$.[11]

Besides Helmholtz-like excitation, where the air in the cavity is coherently pressurized and expanded, standing wave patterns inside the cavity can emerge. The combined effect of all acoustic pressure waves in the cavity volume can create a standing pattern consisting of a fixed number of sinusoidal waves between opposite cavity boundaries. The frequencies for a rectangular box of dimensions $L, D, W$ are:[21]

$$f_{n_x,n_y,n_z} = \frac{c}{2}\sqrt{\left(\frac{n_x}{L}\right)^2 + \left(\frac{n_y}{2D}\right)^2 + \left(\frac{n_z}{W}\right)^2}. \tag{2}$$

## III. Experimental setup

### A. windtunnel model

The experimental geometry consists of a rectangular cavity partially closed off by a rigid overhang either from the upstream or downstream edge of the cavity. The cavity opening is subjected to a flow with a thick (compared to the opening length $\delta$) flat plate boundary layer profile. The aspect ratio of the cavity is large, $\frac{W}{\delta} >> 1$.

For the experiments the vertical tunnel (V-tunnel), located at Delft University of Technology in the Netherlands was used. The V-tunnel is a tunnel with an open test section and a vertical outflow though a circular opening, 0.6 m in diameter. Due to the high contraction ratio of the settling chamber the quality of the airflow is high (low turbulence) and the tunnel is relatively silent.

The model used in the windtunnel is a cavity embedded in a splitter plate which has an elliptic nose cone. Figure 1 gives the dimensions of the cavity and figure 4 shows a photograph of the splitter plate with the embedded cavity. The expected Helmholtz resonance frequency is around 800 Hz and expected base resonance onset velocity is 25 m/s. This is in the velocity range of the used vertical windtunnel (0 to 47 m/s) and is also an interesting velocity to resemble a car door gap (typical car highway speeds).

The boundary layer develops on the first section of the plate. By adjusting the length of the splitter plate and the location of trip wires the boundary layer is controlled in a precise and reproducible way. The splitter plate upstream flat plate section is set to varied between 0.2, 0.3, 0.5, 0.7 and 0.9 m and a 1 mm high zigzag type turbulator strip is located 10 cm from the splitter plate nose.

The cavity itself is constructed out of thick-walled aluminum to ensure enough rigidity to prevent fluid-structure resonance effects. Interchangeable parts are used to alter the neck geometry. The cavity dimensions are given in figure 1. The cavity neck can be equipped with sharp or round edges and a upstream or downstream edge overhang can be implemented, as depicted in figures 2 and 3.

The maximum spanwise width of the cavity is set to 0.5 m, which is smaller than the 0.6 m width of the splitter plate itself. This leaves 5 cm on both sides (shown in figures 1 and 4) to ensure that the end effects of the outlet (the shear layer of the outlet jet) will not reach the cavity region. In this way the flow speed and boundary layer shape remain constant along the whole span of the cavity. The current experiments also include runs with a reduced cavity width of 0.3 m by closing one side with blocks in both the interior and opening. This reduced setup is used to evaluate the effect of the total span on the resonance behavior.

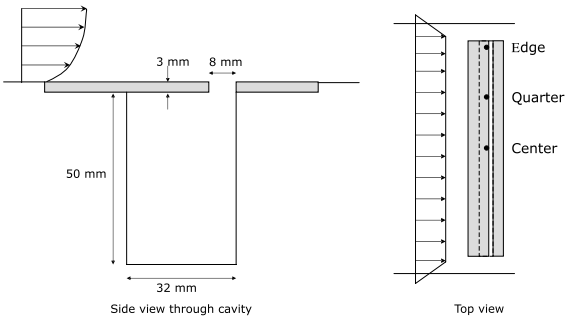


**Figure 1. Cavity dimensions.**

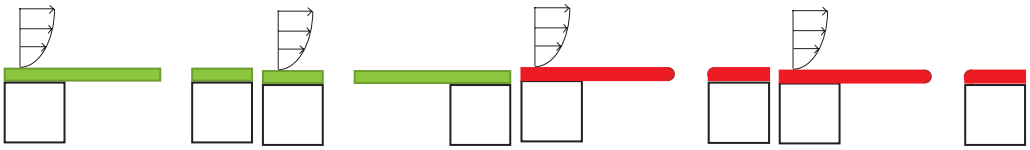

(a) Upstream edge overhang, sharp edges (b) Downstream edge overhang, sharp edges (c) Upstream edge overhang, rounded edges (d) Downstream edge overhang, rounded edges

**Figure 2. Possible cavity neck setups without mixing round and sharp elements**

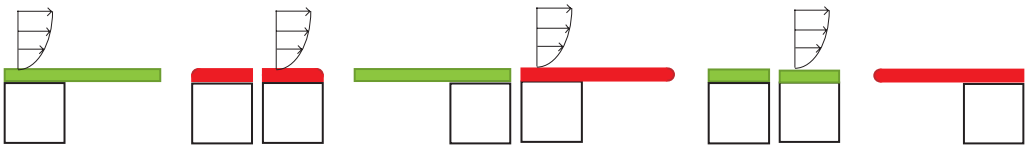

(a) Sharp upstream edge overhang, rounded downstream edge (b) Sharp downstream edge overhang, rounded upstream edge (c) Rounded upstream edge overhang, sharp downstream edge (d) Rounded downstream edge overhang, sharp upstream edge

**Figure 3. Possible cavity neck setups by mixing round and sharp elements**

**Figure 4. The windtunnel model; cavity with embedded splitter plate.**

### B. Measurements

The boundary layer characteristics are measured with a constant temperature hotwire probe. For this, the cavity is closed off. The velocity magnitude in the boundary layer is measured at 25 different heights (with uneven spacing, most measurements in the lower regions), for 4 different flow speeds (20, 24 , 30 and 40 m/s) and 3 spanwise locations (center, quarter and edge of cavity, see figure 1).

Flow runs with open cavity have been performed to measure the flow induced sound pressure levels inside the cavity. The velocity is increased incrementally, up to the wind tunnel limit of approximately 47 m/s. The open cavity flow run experiments use 3 pressure transducers. These are located at different spanwise locations (center, quarter, and edge) on the floor of the cavity, as indicated in figure 1.

In order to evaluate the flow in the opening region, high speed, time resolved particle image velocimetry (PIV) has been used. All setups indicated in figures 2 and 3 have been investigated. PIV is also used to capture the lower boundary layer characteristics and is combined with hotwire results.

The illumination over an area of 25 by 16 mm is provided by a Quantronics Darwin-Duo 527 Nd:YLF laser. The field of view covered the cavity opening and the outer flow boundary layer up to 8 mm in height. The light sheet is positioned steamwise and perpendicular to the plate, with spanwise location 80 mm from the opening edge, as indicated in figure 1. A Photom Fastcam SA1.1 camera (1,024 x 1,024 pixels) is placed at a 90 degree angle with the illumination, and captures 1024x512 images. The illumination and recording devices are synchronized and controlled by a LaVision programmable timing unit (PTU v9) controlled by DaVis 7.3 software. Each measurement consists of 1000 image pairs at a recording frequency of 6000 Hz, which is sufficient to capture the temporal behavior of the flow (at approximately eight samples per resonance cycle). The double pulse interval is varied between 8 and 15 microseconds, depending on the velocity. The chosen magnification yields a typical digital resolution of 40 pixels/mm. The images were analyzed with the LaVision Davis 7.3 software, using a multi-step cross-correlation with a final interrogation window size of 16 by 16 pixels (0.4 by 0.4 $mm^2$) with 75% overlap. A sample image is given in figure 5.

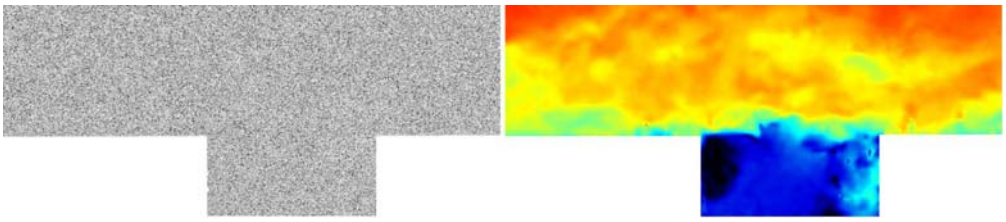

**Figure 5. Sample recording after initial image processing (left) and flow result showing velcoity magnitude from 0 m/s till $U_\infty$ (right).**

## IV. Numerical setup: Lattice Boltzmann Method

Numerical simulation results of flow and acoustics are obtained using the Lattice Boltzmann Method (LBM).[22] LBM is an alternative numerical method to traditional CFD for simulating complex fluid flows. Unlike conventional methods based on macroscopic continuum equations, the LBM starts from mesoscopic kinetic equations, i.e., the Boltzmann equation, to determine macroscopic fluid dynamics. The commercial LBM based package PowerFLOW is used.

The lattice Boltzmann equation has the following form:

$$f_i\left(\vec{x}+\vec{c_i}\Delta t, t+\Delta t\right) - f_i\left(\vec{x}, t\right) = C_i\left(\vec{x}, t\right), \tag{3}$$

where $f_i$ is the particle distribution function moving in the $i$th direction, according to a finite set of the discrete velocity vectors $\{\vec{c_i} : i = 0, ..., N\}$. $\vec{c_i}\Delta t$ and $\Delta t$ are space and time increments respectively. The collision term on the right hand side of Eq. (3) adopts the simplest and also the most popular form known as the Bhatnagar-Cross-Krook (BGK) form:[23] :

$$C_i\left(\vec{x}, t\right) = -\frac{1}{\tau}\left[f_i\left(\vec{x}, t\right) - f_i^{eq}\left(\vec{x}, t\right)\right] \tag{4}$$

Here $\tau$ is the relaxation time parameter, and $f_i^{eq}$ is the local equilibrium distribution function, which

depends on local hydrodynamic properties. The basic hydrodynamic quantities, such as fluid density $\rho$ and velocity $\vec{u}$ , are obtained through moment summations over the velocity vectors; i.e.

$$\rho\left(\vec{x},t\right)=\sum_{i}f_{i}\left(\vec{x},t\right),\ \rho\vec{u}\left(\vec{x},t\right)=\sum_{i}\vec{c}_{i}f_{i}\left(\vec{x},t\right) \tag{5}$$

In the low frequency and long-wave-length limit, for a suitable choice of the set of discrete velocity vectors, one can recover the compressible Navier-Stokes equations through the Chapman-Enskog expansion for Mach numbers less than (approximately) 0.4.[22] The resulting equation of state obeys the ideal gas law, $p=\rho RT$. The kinematic viscosity of the fluid is related to the relaxation time parameter, $\tau$ , by:[24]

$$\nu=\left(\tau-1/2\right)T \tag{6}$$

The combination of Eq. (3) to (6) forms the LBM scheme.

By recovering the compressible Navier-Stokes equations, including an ideal gas equation of state, LBM also inherently recovers acoustics. Some fundamental aeroacoustic capabilities of the scheme have been studied before, such as wave propagation and compressible behavior.[25,26] In these cases the code has proven itself capable of correctly simulating these acoustics related problems. Examples of the use of the Lattice Boltzmann scheme in acoustics are simulation of radiation from waveguides,,[27] acoustic pulses in flows and duct aeroacoustics,[28] and side branches.[26]

Lattice Boltzmann equation is solved on a grid composed of cubic volumetric elements, and variable resolution is allowed, where the grid size changes by a factor of two for adjacent resolution regions.

Powerflow uses a $K-\epsilon$ RNG turbulence model with a local model reduction based on swirl and strain to allow large vortices to be simulated directly. A turbulent wall slip model is implemented as well.

## V. Experimental results

In this section the obtained experimental results are presented.

### A. Incoming boundary layer

The boundary layer measurement results are used to check the boundary layer height, shape and fluctuations. Also, measurements are done to check that the flow properties are constant across the entire span.

The profiles for the mean and root mean squared (RMS) fluctuation profiles of velocity magnitude (more accurately the vector addition of the streamwise and vertical velocity component) are given in figure 6 for the center location (middle of the cavity neck opening, 25 cm from the opening edge) of a 0.7 m plate flow. The other two locations, quarter (12.5 cm from the opening edge) and edge have similar boundary layer properties. The figures show that the boundary layer properties remain similar during the flow sweep. There is a mild thickness decrease with increasing velocity due to Reynolds effects.[29]

Figure 7 indicates the change in boundary layer characteristics due to the increasing used plate lengths. The PIV results are also presented in this figure. One can see that the PIV results match the hotwire results well. The PIV results are used to obtain the lower boundary layer profile and the hotwire results are used for the upper boundary layer profile and the intermediate plate thickness variations. The shape of the boundary layer is a typical turbulent flat plate one, and the relative shape does not change much with varying boundary layer thickness. This can also be observed by evaluating the boundary layer integral properties.

The following integral properties are evaluated; the displacement thickness $\delta^*$, the momentum thickness $\theta$, the shape factor $H$ and the height at 99% of the mean flow $\delta_{99}$.[29]

The displacement thickness $\delta^*$, momentum thickness $\theta$, and shape factor $H$ are defined as:

$$\delta^*=\int_0^\infty\left(1-\frac{\bar{u}}{U_e}\right)dy, \tag{7}$$

$$\theta=\int_0^\infty\frac{\bar{u}}{U_e}\left(1-\frac{\bar{u}}{U_e}\right)dy, \tag{8}$$

$$H=\frac{\delta^*}{\theta}, \tag{9}$$

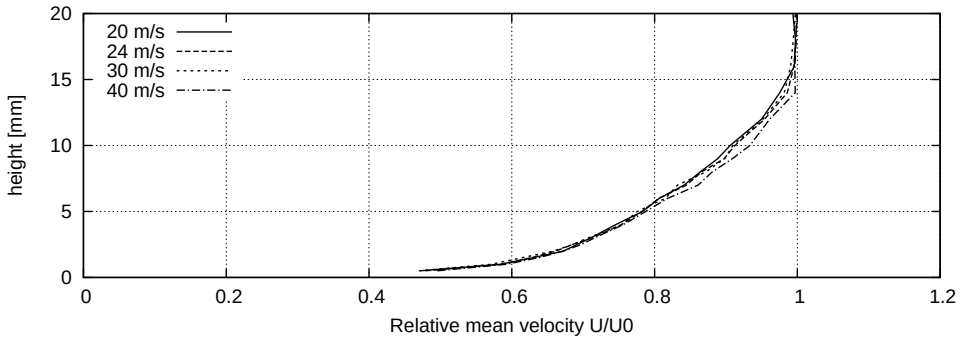


(a) $\bar{u}/u_\infty$

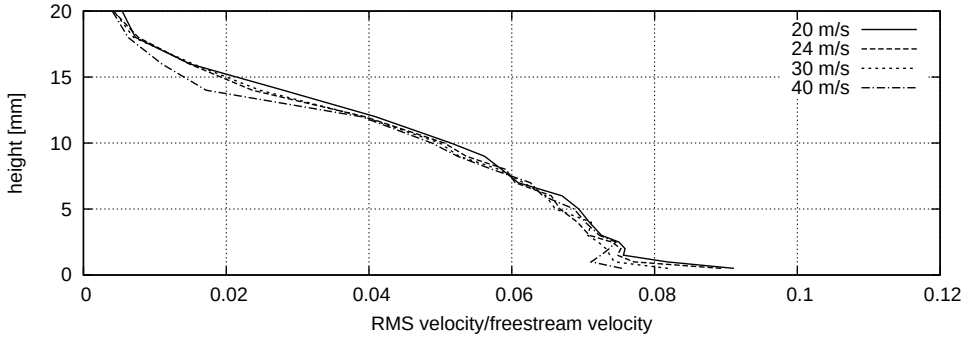


(b) $\overline{u'^2}/u_\infty$

**Figure 6. Boundary layer mean (top) and rms (bottom) profiles of velocity magnitude**

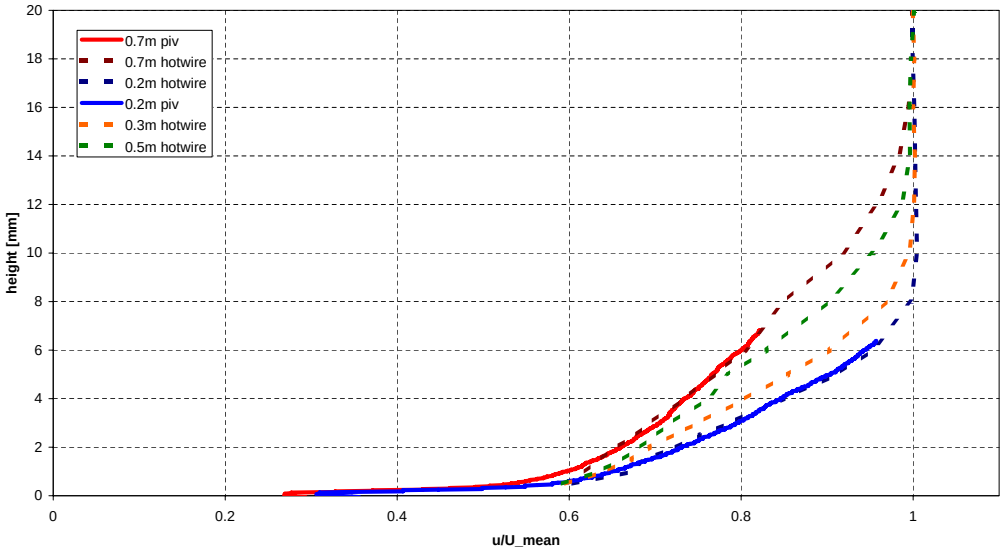


**Figure 7. Experimental boundary layer mean profiles for 4 different plate lengths**

where $U_e$ is the velocity outside the boundary layer and $\bar{u}$ the local mean velocity magnitude at height $y$.

Table 1 shows the influence of velocity for the 0.7m plate length and includes boundary layer data for 3 different spanwise locations to indicate the consistency across the span. Table 2 shows the boundary layer properties for the different plate lengths. On can see that the shape factor stays in the same range, indicating shape similarity for the profiles.

**Table 1. Overview of boundary layer properties for 0.7m plate length, center/quarter/edge location in span as indicated in figure 1**

| flow velocity $[m/s]$ | $\delta^*$ | $\theta$ | H | $\delta_{99}$ |
|---|---|---|---|---|
| 20 | 2.46 | 1.80 | 1.36 | 15.4 |
| 24 | 2.40 | 1.75 | 1.37 | 14.9 |
| 30 | 2.46 | 1.79 | 1.38 | 15.9 |
| 40 | 2.24 | 1.64 | 1.37 | 13.6 |

**Table 2. Overview of boundary layer properties for different plate lengths at 24 m/s, center location. Please note that 0.9m plate values are estimated using all other plate length data.**

| Plate length $[m]$ | $\delta^*$ | $\theta$ | H | $\delta_{99}$ |
|---|---|---|---|---|
| 0.2 | 1.16 | 0.85 | 1.36 | 7.6 |
| 0.3 | 1.47 | 1.08 | 1.36 | 9.6 |
| 0.5 | 1.96 | 1.46 | 1.34 | 12.7 |
| 0.7 | 2.40 | 1.75 | 1.37 | 14.9 |
| 0.9 (estimated) | 2.81 | 2.05 | 1.36 | 17.3 |

### B. Unsteady pressure in the cavity

The cavity flow induced resonance is investigated by measuring the internal pressure response. In the current section the results for the upstream overhang with sharp edges is presented. The upstream flat plate length is set to 0.7 m.

The flow velocity is increased incrementally. The internal probe sound pressure levels of these velocity sweeps are gathered in spectrograms and given in figure 8 for all 3 probe locations. The frequency of the excitation is shown at the vertical axis and the free stream velocity on the horizontal one. The amplitude of the excitation is in dB is indicated by level.

The figure shows several resonating modes with increasing velocity and increasing frequency. The first resonance is visible at all probe locations whereas for the higher modes some are not. This indicates a spanwise variation in the higher resonance modes.

From figure 8 it is found that all the center points of the excitation modes show a linear relation between frequency and velocity. The Strouhal number $Sr = \frac{fL}{U_\infty}$ corresponding to this is approximately 0.3, indicating that all modes are hydrodynamically excited by the first stage Rossiter mode.[1] No excitations of the second stage Rossiter mode ($Sr \approx 0.7$) are present, although low amplitude onsets of resonance for this Strouhal number can be observed in the upper left part of the figures as light horizontal lines.

Even though the acoustic pressure amplitudes can be around 120 dB, it can be calculated that the energy transfer from flow to acoustics is low.[4] In figure 9 the maximum acoustic pressure amplitude is $|p| = 30$ Pa and $|p| = 100$ Pa for the 22 and 42 m/s case respectively. The estimated acoustic velocity amplitude $|u_{ac}|$ in the neck region for a lumped mass system can be estimated by:

$$\frac{|u_{ac}|}{U_0} \approx \frac{1}{U_0}\frac{V_{cav}}{\rho_0 S}\left|\frac{d\rho}{dt}\right| = \frac{1}{U_0}\frac{L}{\delta}\frac{2\pi f D}{c}\frac{|p|}{\rho_0 c} = \frac{1}{2}\sqrt{\frac{V_{cav}}{V_m}}\frac{|p|}{p_{dyn}}\frac{U_0}{c} \approx \sqrt{2}\frac{|p|}{p_{dyn}}\frac{U_0}{c}, \tag{10}$$

with $S = \delta W$ the area of the neck opening, $V_{cav} = LDW$ the cavity volume, $V_m = \delta H' W$ the modified volume of the opening section and $p_{dyn} = \frac{1}{2}\rho U_0^2$ the dynamic pressure. Also $dp = c^2 d\rho$ with $c$ the speed of sound is used.

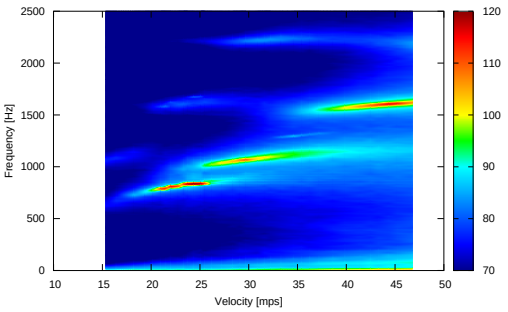


(a) Center location

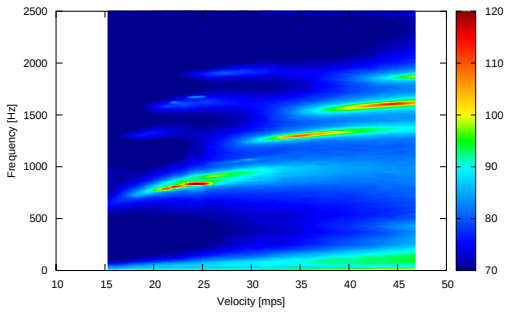


(b) Quarter location

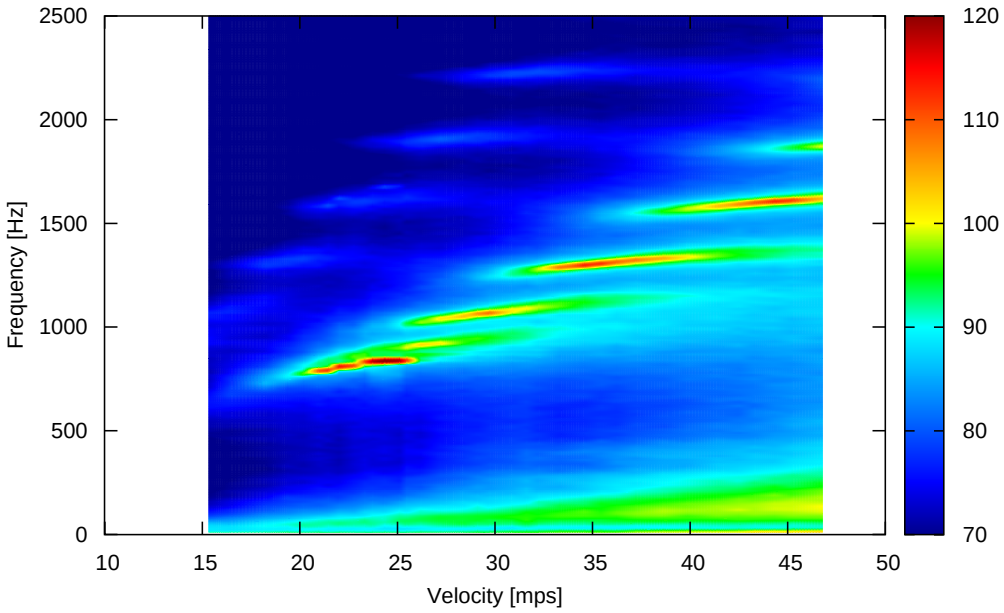


(c) Edge location

**Figure 8. (Color online) Spectrograms of the three internal pressure probes, level by sound pressure** $[dB]$

Substituting $f = 800$ Hz, $U_0 = 25$ m/s, $|p| = 25$ Pa will give $\frac{|u_{ac}|}{U_0} \approx 1 \cdot 10^{-2}$ and substituting $f = 1600$ Hz, $U_0 = 42$ m/s, $|p| = 100$ Pa will give $\frac{|u_{ac}|}{U_0} \approx 3 \cdot 10^{-2}$. The low acoustical amplitude makes the lock-on hard to predict.[30]

The higher modes are not simple pure standing waves according to Eq. (2), because standing waves that match the observed spanwise pressure variations do not match the observed frequencies. This is indicated in table 3, where frequencies of standing wave modes that match the phases and node locations indicated in figures 8 and 9 are compared to the experimentally observed frequencies. $\lambda$ is the standing mode wavelength. Note that in this table the coherently excited base mode does not match any standing wave mode shape.

**Table 3. Comparison flow run mode frequencies with pure standing wave modes.**

| Mode | Exp. freq. [Hz] | Shape matching st. wave number $n_{st} = 2W/\lambda$ | St. wave freq. [Hz] |
|---|---|---|---|
| 1 | 830 | n/a | n/a |
| 2 | 900 | 1 | 340 |
| 3 | 1050 | 2 | 680 |
| 4 | 1300 | 3 | 1020 |
| 5 | 1600 | 4 | 1360 |
| 6 | 1900 | 5 | 1700 |

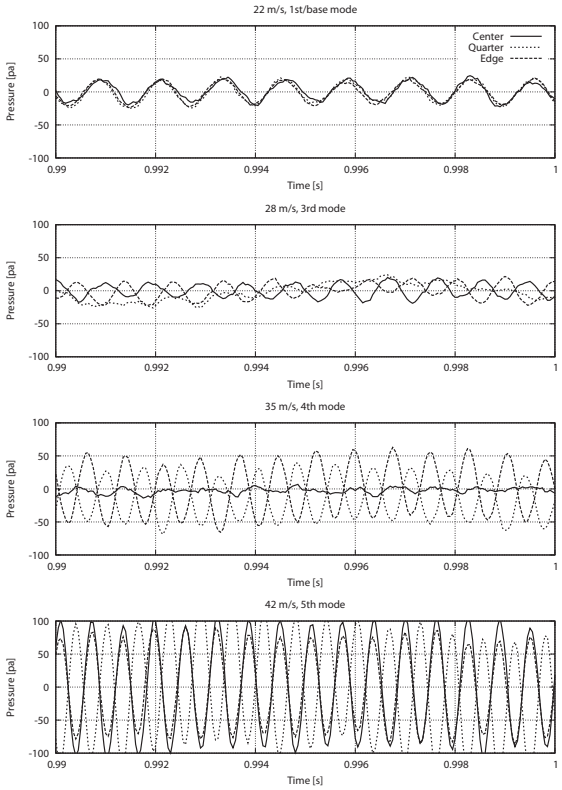


**Figure 9. Pressure time series of the 3 cavity internal probes for some of the observed modes.**

In order to investigate the higher modes with spanwise variation in more detail, flow runs with a reduced span of 0.3 m are conducted. All other dimensions remained the same compared to the 0.5 m span experiments. The spectrograms of the flow induced response for the edge probe is given in figure 10. The modes are all excited by the first stage Rossiter mode. The most noticeable differences compared to the 0.5 m span runs of the lower graph of figure 8 are the lower base mode resonance amplitude and location of the higher modes in the diagram.

The base mode has a frequency of around 800 Hz, which is the same as for the 0.5 m span cavity. This confirms that the slender Helmholtz added length $l$ of Eq. (1) is independent of the cavity width $W$. By comparing the higher modes in the lower graph of figure 8 with figure 10, a distinct influence of the spanwise width can be observed. The higher modes are shifted to larger velocities and have higher frequencies. For example the second mode shifted from 26 m/s, 900 Hz to 28 m/s, 1000 Hz and the third mode shifted from 28 m/s, 1100 Hz to 34 m/s, 1400 Hz. The shifts cause less modes to appear in the used velocity interval of 10 m/s to 47 m/s. The smaller span runs reveal strong dependence of the higher mode excitation frequency on the spanwise length. The next section describes an experimental and numerical acoustic response test that will be used to obtain the exact mode shape of the observed modes.

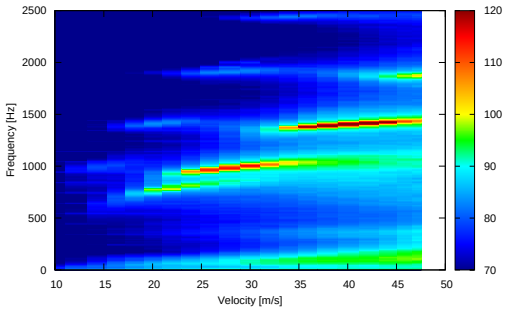


**Figure 10. (Color online) Spectogram of flow run with a 0.3 m span, edge location internal cavity probe, level by sound pressure** $[dB]$**.**

### C. Shear layer characteristics

The time-resolved flow field is given in figure 11 for a resonating configuration a (upstream edge overhang, sharp edges). The boundary layer is highly turbulent and interacts with the shear layer dynamics. The shear layers shows both shear flapping motion (first half) and vortex roll up (second half). The generated vorticity gets partly entrapped into the cavity due to the interaction with the downstream edge.

## VI. Analysis: base mode

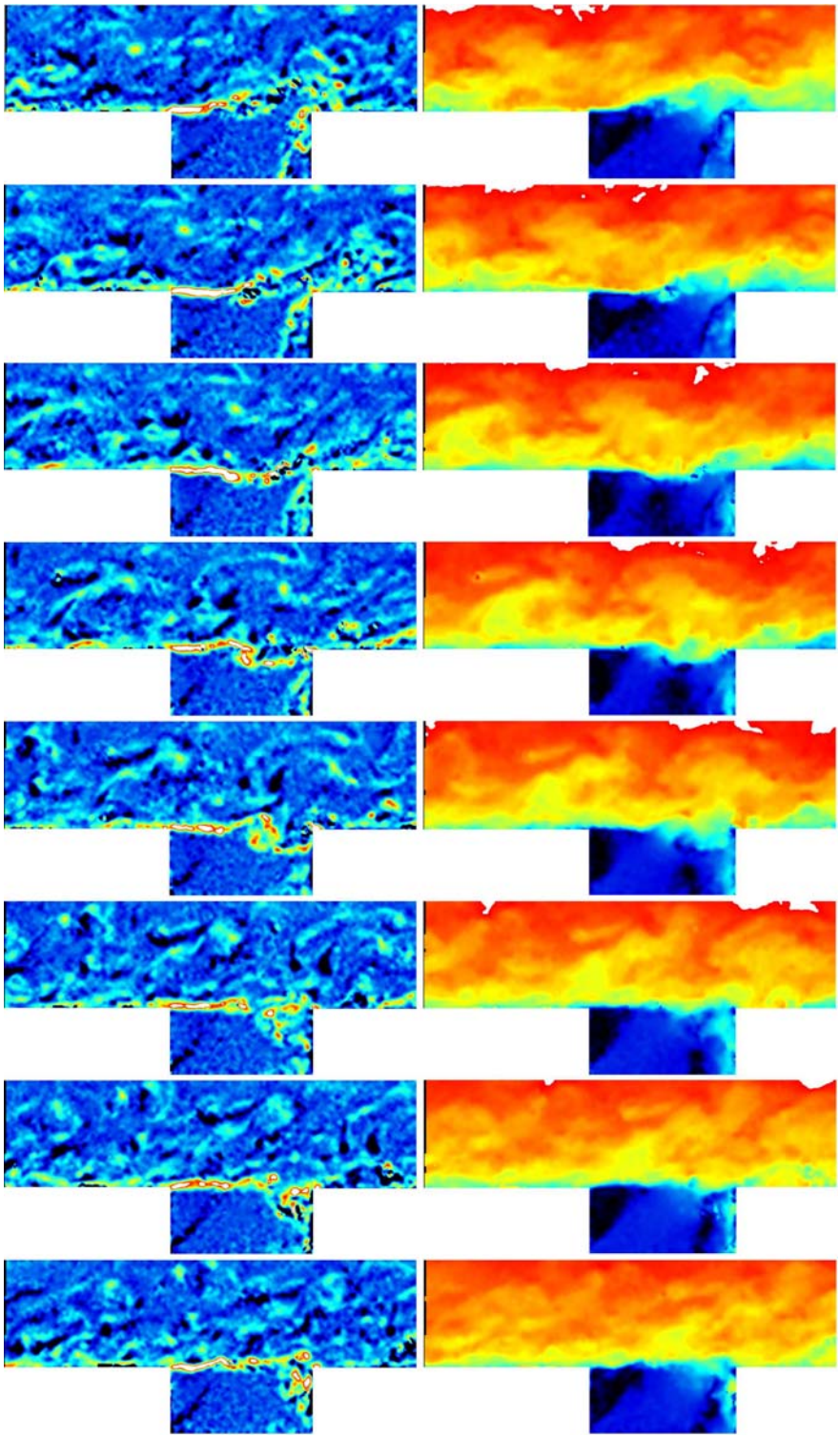

**Figure 11. One cycle of time-resolved PIV images, spanwise vorticity (range -5000 - 30000 $s^{-1}$) and velocity magnitude (range 0 m/s - $U_\infty$). configuration a (upstream edge overhang, sharp edges) used.**

### A. Influence of relevant parameters

Five main parameters have been varied to investigate the sensitivity of the cavity to lock-on. First of all the velocity varied. Due to the fact that in literature thick boundary layers show a resistance to lock-on into resonance, the boundary layer height is varied. the last three parameters concern the geometry of the resonator opening. The overhang lip location is varied between a upstream edge overhang and a downstream edge one. Furthermore the upstream edge and downstream edge rounding has been modified independently between a sharp edge and a semi-arc roundoff. The sharps edges have been shown to promote resonance in the current cavity geometries,[16,17] whereas the rounded edges better resemble real world gaps.

Figures 12 and 14 show the influence of the lip opening to the excitation results. Figures 13 and 15 are the scaled representations of the amplitudes, indicating the ratio of the acoustic velocity to the freestream velocity.[4] One can clearly see that the degree of acoustic lock-on is relatively low, less than 1 percent in most cases. This makes lock-on hard to predict. The scaled representation also shows non-resonant areas as horizontal lines.

The effect of boundary layer thickness is included in the figures. With increasing boundary layer thickness, the amplitudes diminish. 0.9 m plate length shows no resonance lock-on anymore for all modes. Interestingly, the various geometries show different resonance onset boundary layer thicknesses.

By comparing the geometries, only 3 setups show consistent resonance lock-on: upstream edge overhang with sharp edges, upstream edge overhang with round edges and upstream edge overhang mixed with round overhang and sharp downstream edge. By evaluating the figures one can draw the following conclusions:

- A downstream edge overhang does not observe resonance behavior
- with increasing boundary layer thickness, lock-on modes diminish. The cutoff boundary layer height is geometry dependent
- Rounding the downstream edge will diminish the lock-on amplitude.
- Rounding the upstream edge will promote the lock-on amplitude.
- Only upstream edge overhang, sharp edges shows higher modes with spanwise variations

These items will be analyzed separately in the next sections.

Besides the lock-on behavior, scaled figures 13 and 15 reveal an influence on the broadband behavior as well. table 4 summarizes the broadband acoustic velocity. The table indicates that rounding of upstream as well as downstream edges increases the passive response of the cavity. the effect of the upstream edge is larger.

| | upstream edge sharp | upstream edge round |
|---|---|---|
| downstream edge sharp | 0.02% | 0.03% |
| downstream edge round | 0.025% | 0.035% |

**Table 4. Effect of broadband fluctuations, downstream edge overhang. Table indicates average $u_{ac}/U_\infty$, for the velocity range of 30-45 $m/s$.**

### B. Influence of boundary layer

The flow shown in figure 11 has a lot of turbulent structures that interact with the shear layer. It is believed that these structures influence the resonance behavior in two ways. First of all, the turbulent structuctes break up the spanwise coherency of the shear layer, thus reducing resonance amplitude. Secondly the structures directly perturb the cavity, enabling resonance onset. The balance between there opposite effects is further investigated using numerical simulations in section VIII.

### C. Influence of overhang location

Time averaged PIV results are used to explain the difference in response behavior between a upstream and downstream edge overhang. When comparing the flow in the cavity opening, an interesting difference can be observed. Figure 16 shows the mean flow patterns for the sharp edges upstream and downstream edge

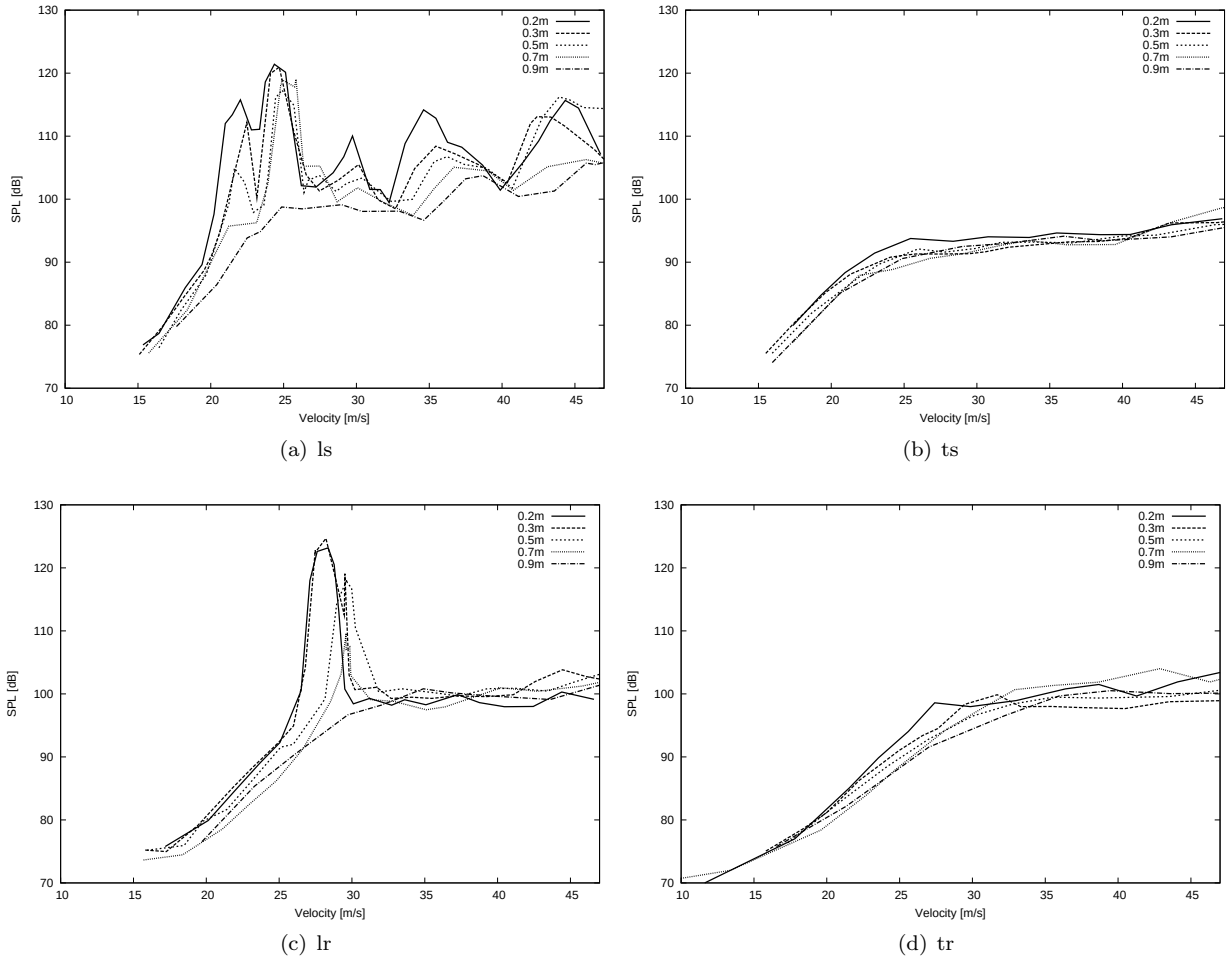


(a) ls (b) ts

(c) lr (d) tr

**Figure 12. Maximum probes excitation amplitude all non-mixed lip configurations**

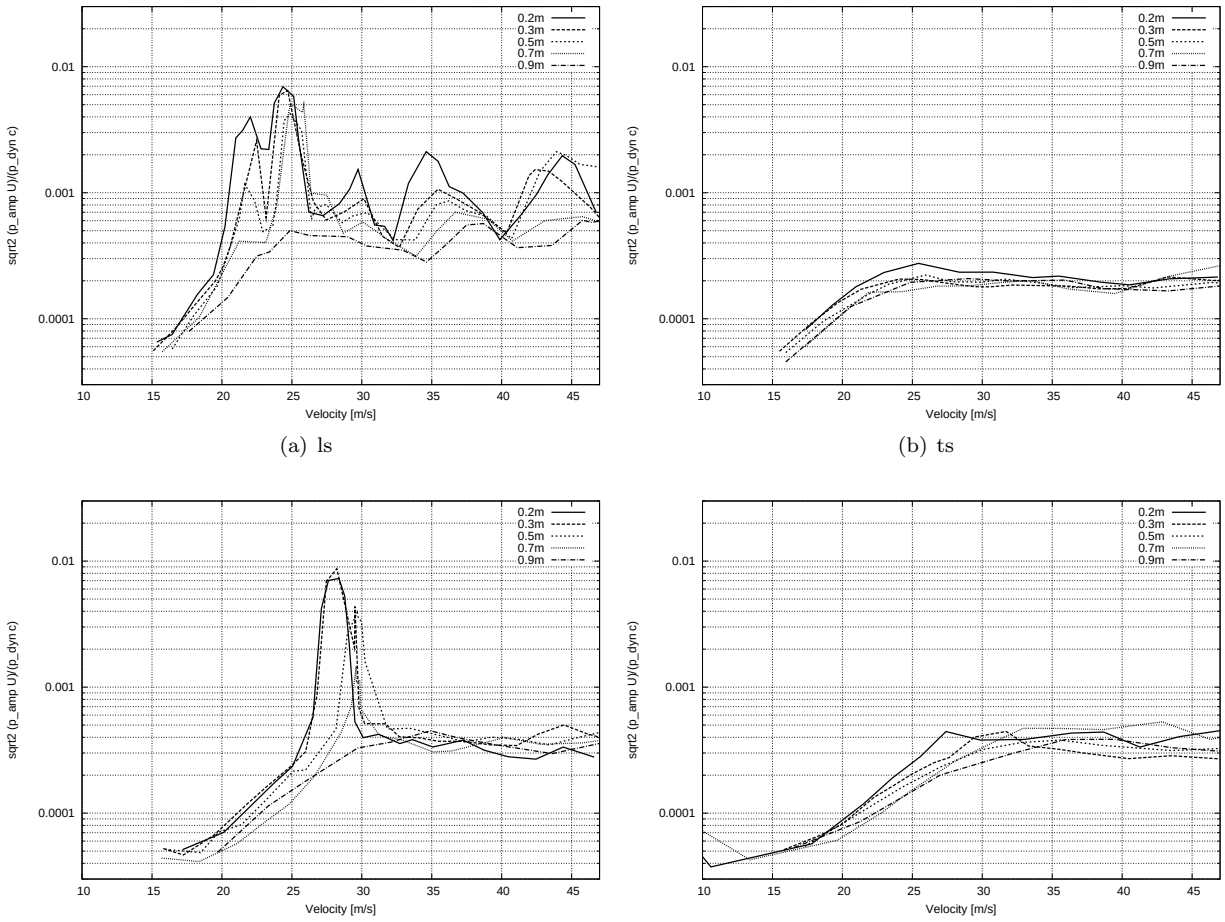


(a) ls (b) ts

(c) lr (d) tr

**Figure 13. Maximum probes excitation amplitude all non-mixed lip configurations, level scaled by $\sqrt{2}\frac{p_{ac}}{p_{dyn}}\frac{U_\infty}{c}$, indicating the ratio of acoustic velocity in the neck compared to the freestream velocity.**

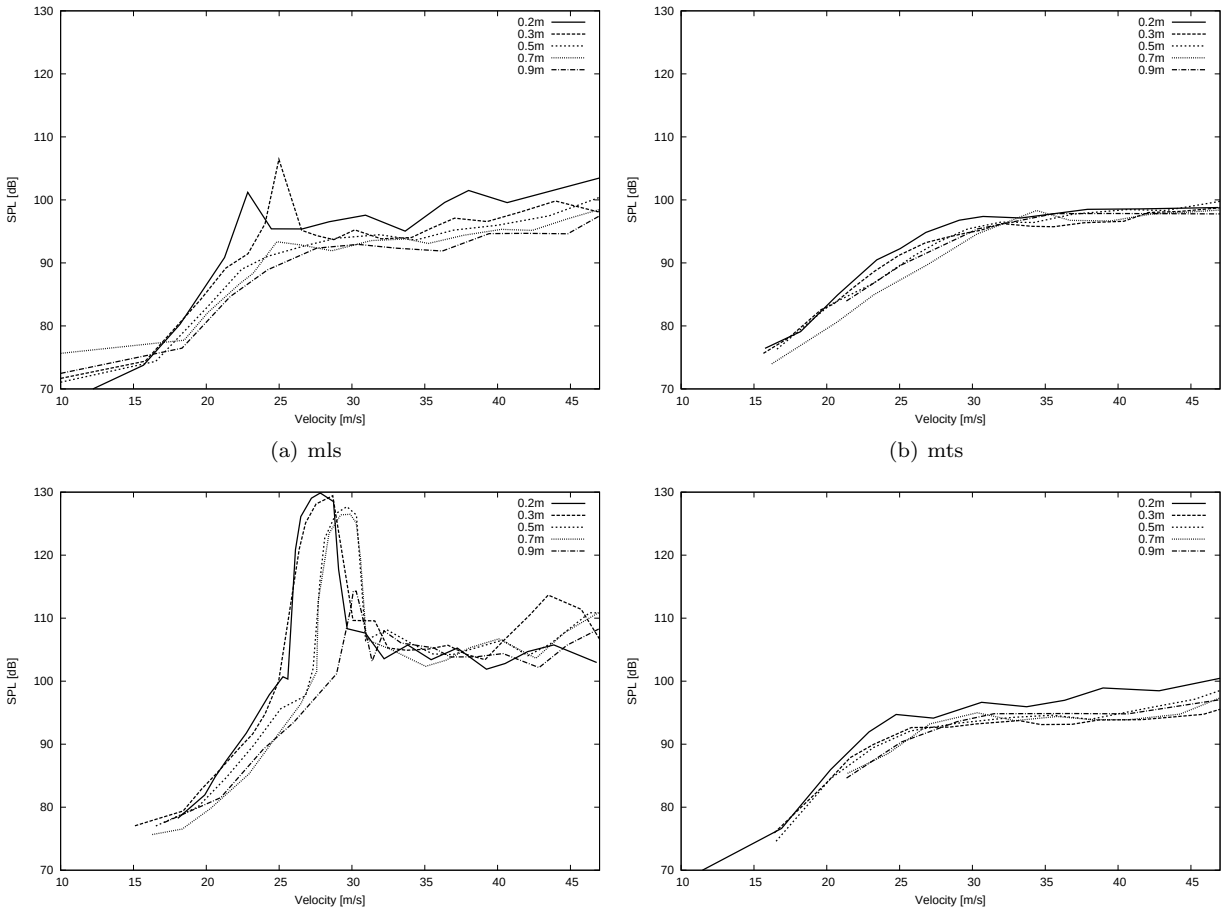


(a) mls (b) mts

(c) mlr (d) mtr

**Figure 14. Maximum probes excitation amplitude all mixed lip configurations**

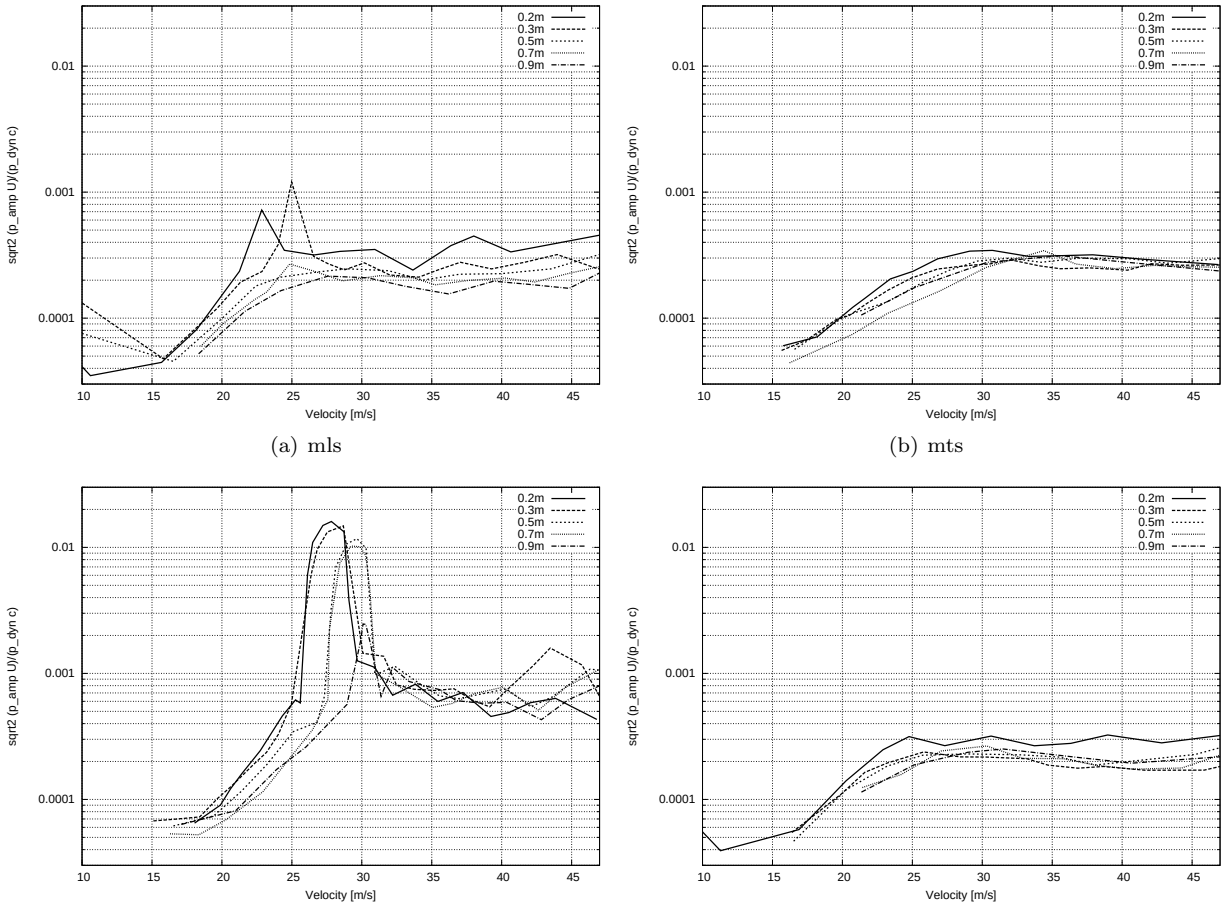


(a) mls (b) mts

(c) mlr (d) mtr

**Figure 15. Maximum probes excitation amplitude all mixed lip configurations, level scaled by $\sqrt{2}\frac{p_{ac}}{p_{dyn}}\frac{U_\infty}{c}$, indicating the ratio of acoustic velocity in the neck compared to the freestream velocity.**

overhang cavities. The cavity driven flow in the opening for the downstream edge overhang shows a large steady trapped vortex, whereas the upstream edge overhang shows a jet-like internal flow pattern with a separation region at the upstream sidewall. This influences the shear layer over the opening. The effective shear is much lower for the downstream edge geometry and therefore the shear layer can be more stable.

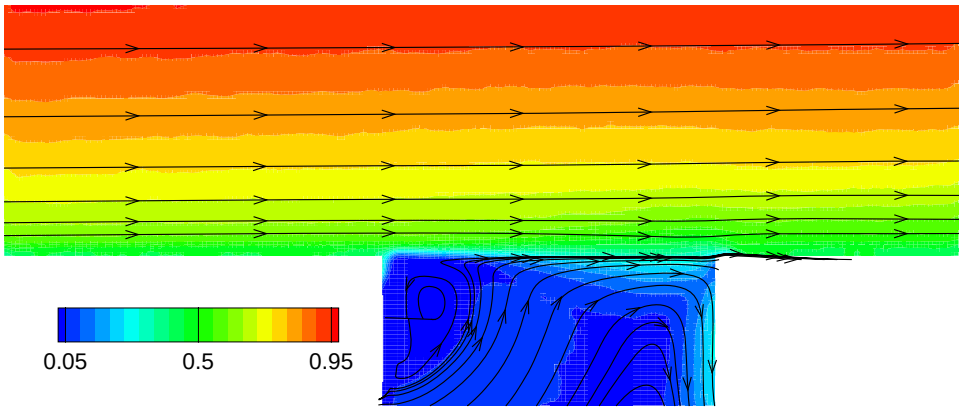


**D.**

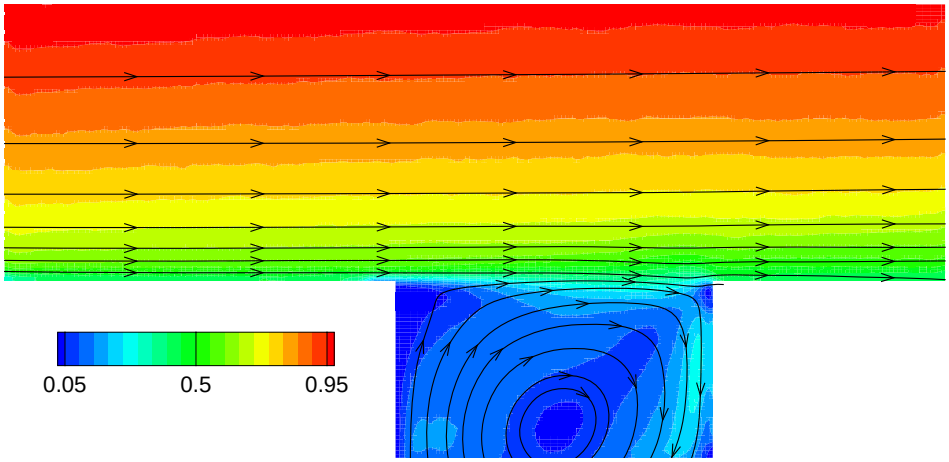


**E.**

**Figure 16. Mean flow patterns in the cavity opening**

Figure 17 shows the streamwise velocity distribution in the opening, where the lid driven flow component of the downstream overhang case is accounting for a flow of about $0.1U$ in the cavity. This can greatly modify the stability behavior of the shear layer. The effective shear is given in figure 18. Here one can clearly see the shear reduction in the first section of the shear layer for the downstream overhang case. The vorticity thickness is changed only slightly when scaled with respect to the effective shear velocity.

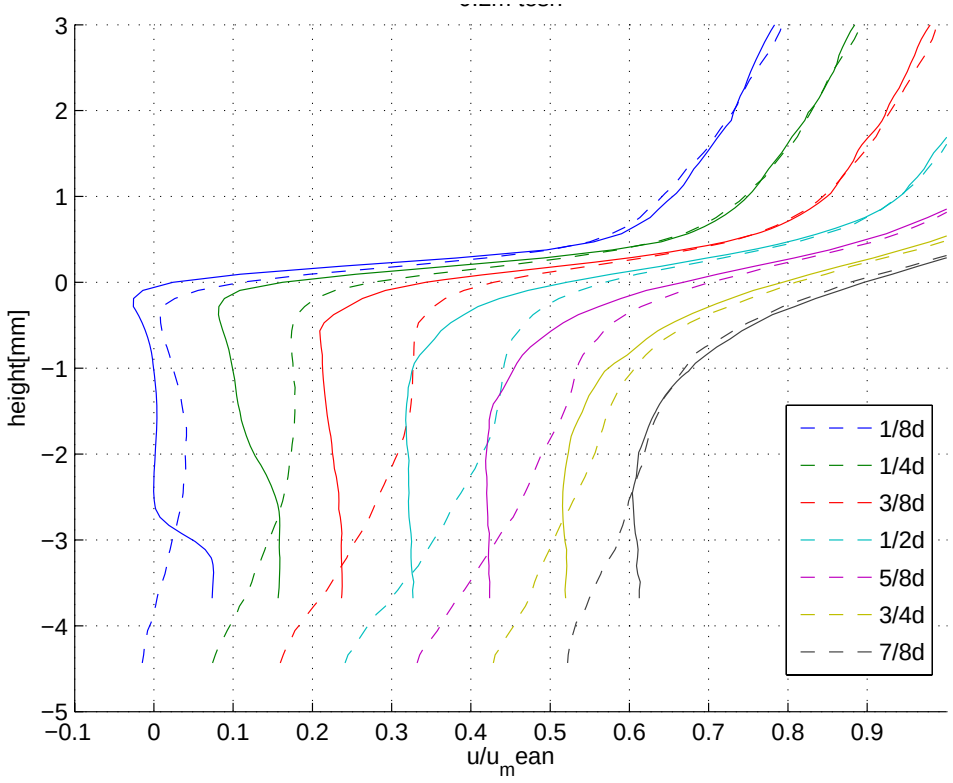


**Figure 17. Comparison mean shear layer patterns over the cavity opening, sharp edges, 0.2m upstream plate length, for upstream overhang (solid) and downstream overhang (dashed). Graphs are offset by 0.1** $u/U_\infty$

.

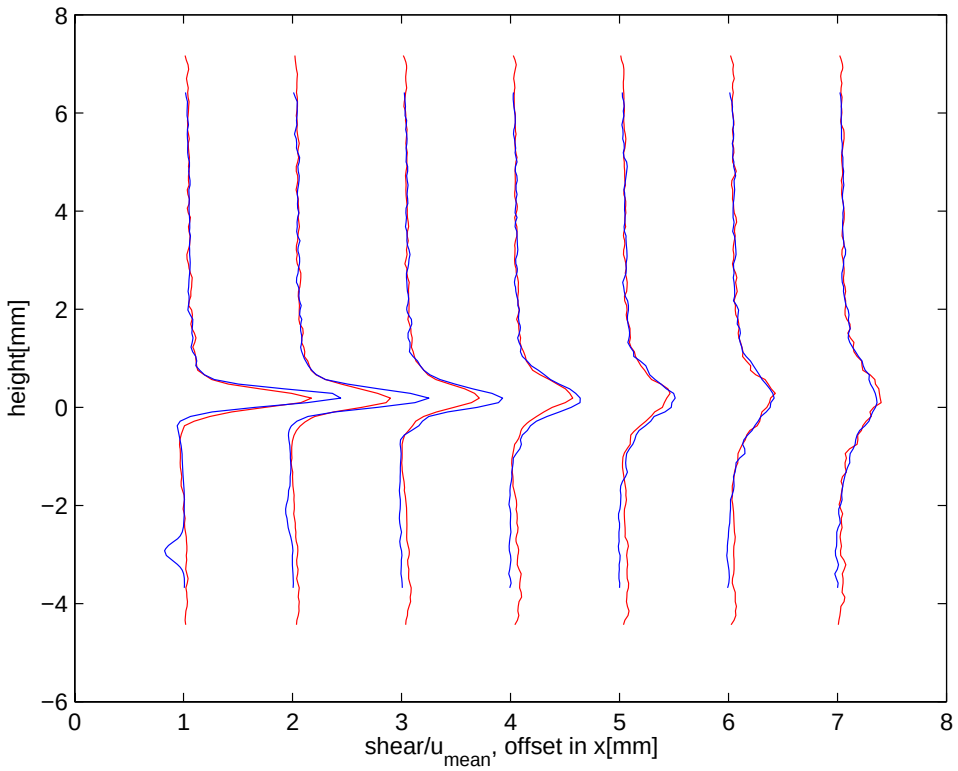


**Figure 18. Comparison effective shear divided by free stream velocity $\frac{d(u/U_\infty)}{dx}$ over the cavity opening, measured with $\frac{1}{8}\delta$ increments for upstream overhang (blue) and downstream overhang (red). Graphs are offset by 1 $m^{-1}$.**

### F. Effect of downstream edge rounding

As previously indicated, the resonance behavior is very sensitive to the downstream edge geometry. Rounding of the downstream edge will reduce or even diminish the resonance behavior. This has already been indicated in literature, where vortex-edge interaction plays a critical role.

In figure 19, it is observed that the y-location of the stagnation point is shifted downwards with rounding of the downstream edge. An anlogy of a y-shifted knive edge is employed to explain the feedback behavior. Compared to a infinitely thin knife edge ($y_{stagation} = 0mm$, the stagnation point of the sharp edged cases is also lower, but not nearly as much as the cases with rounded downstream edges. The shift in stagnation point will influence the vortex entrapment into the cavity which in turn influences the acoustic feedback of the resonator. A sharp downstream edge causes more vortex entrapment for a given shear layer deflection, explaining the increased lock-on amplitude of the sharp downstream edge geometry.

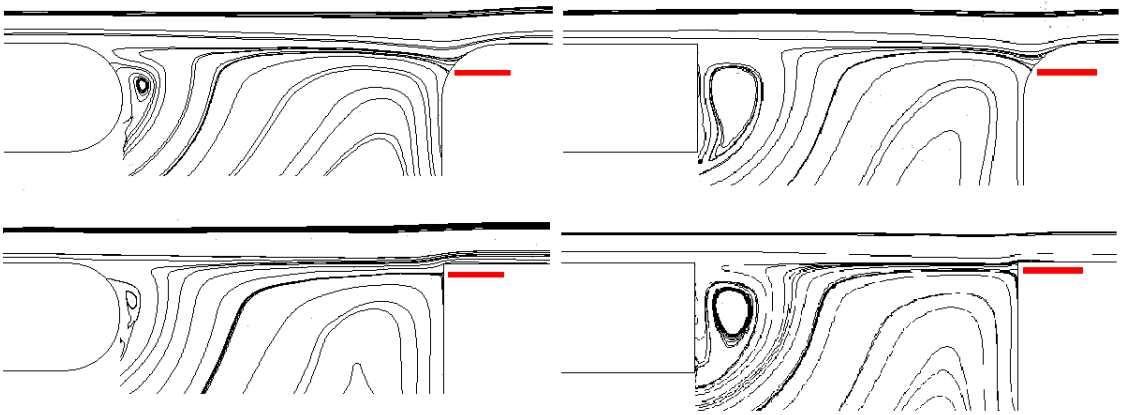

**Figure 19. Streamlines of mean flow with focus on the downstream edge, indicating a modified stagnation point height (shown as red bars) due to the downstream edge geometry.**

### G. Effect of upstream edge rounding

By comparing the maximum lock-on amplitude in figures 13 and 15 one can see the rounding of the upstream edge leads to promotion of resonance lock-on amplitude.

As shown in figure 19, the mean flow is only deflected slightly more into the cavity for rounded upstream edges. Therefore this would not fully explain the increased observed amplitudes

Another hypothesis is that the free separation point of the rounded edge versus the fixed kutta condition induced point of the sharp edge will decrease the stability of the shear layer and allow it to be more sensitive to pressure and velocity perturbations. This is confirmed by examining the rms profiles of the shear layer characteristic scaled with the excitation amplitude for the non-resonating cases in figure 20. One can see that not only the shear layer shows more fluctuations in the first section, but also that an effective extra streamwise length promotes large delfections at the downstream edge and thus more entrapment of vortices into the resonator. The shear layer has more time to grow unstable.

## VII. Analysis: spanwise variations

The spanwise variations observed for the upstream edge overhang, sharp edges case are now more closely investigated using acoustic testing of the cavity.

### A. Acoustic response test

A numerical and the experimental acoustic response test (ART) is performed. An acoustic response test provides the acoustic reaction of the cavity setup in the absence of flow. The numerical simulation is used to obtain the exact mode shapes of the cavity resonances. The experimental ART is used to validate the numerical results. The Lattice boltzmann method described in section IV is used in absence of mean flow.

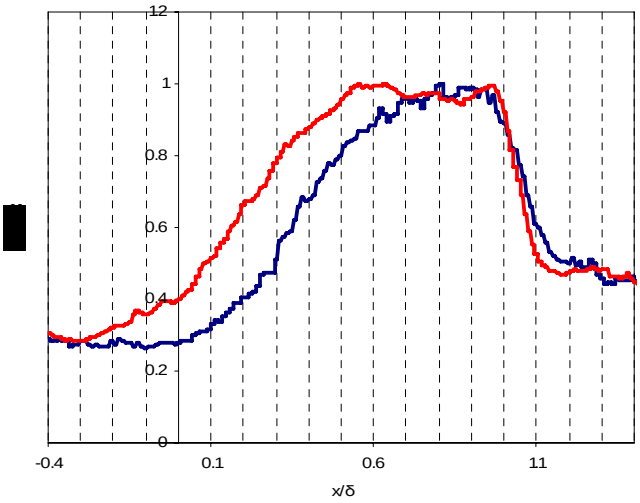


**Figure 20. y-velocity rms profiles in a streamwise rake over the shear layer, 0.5 mm above the opening, scaled with maximum observed y-velocity fluctuation. red rounded upstream edge, blue sharp upstream edge.**

In an ART external speakers emitting a white noise signal are used to excite the cavity in the absence of flow. Microphones inside and outside gather the sound pressure level data.

The excitation of the cavity can be quantified using the complex transfer function. This is the complex ratio of the sound pressure spectrum inside the cavity to a reference outside the cavity. The resulting complex function in frequency is divided by the complex transfer function of a closed cavity where both the main and reference probe are outside. This last extra step provides a frequency dependent scaling to compensate for transfer losses of sound from the speaker toward the cavity region.

Two important properties of Helmholtz resonators are the resonance frequency $f_H$ and the quality factor, $Q$. The resonance frequency is the frequency at which the strongest resonance might occur. The Q-factor describes the sharpness of the resonance peak (as a function of frequency) and can be related to the acoustic impedance of the resonator. The quality factor is defined as:

$$Q = \frac{f_H}{f_2 - f_1}, \tag{11}$$

with $f_1$ and $f_2$ frequencies at half the amplitude of the resonance frequency, where $f_1 < f_H$ and $f_2 > f_H$.

The experimental and numerical complex transfer ratios are compared with an analytical model for a resonator in order to obtain the resonance frequency $f_H$ and quality factor $Q$. The analytical model is fitted with the results using a L2 vector fit in both phase and magnitude. The analytical expression for the transfer magnitude $\|H(f)\|$ is:[9]

$$\|H(f)\| = \frac{1}{k\sqrt{\left(1-(f/f_H)^2\right)^2 + 4D^2\,(f/f_H)^2}} \tag{12}$$

with $k$ the system stiffness and $D$ the damping. The quality factor is related to the damping by $Q = \frac{1}{2D}$.

Both the simulated and experimental ART has the same setup and two-step approach. The full cavity 3d model is included in the simulation and there is no flow present. Two speakers, each with their own independent white noise signal, are used in the numerical setup. Both are positioned at a distance of 2 meters from the cavity (same as in experiment) and are relatively close to each other (30 cm between speaker centers). Both the experimental and numerical setup included 2 speakers to ensure excitation of the modes with spanwise variation.

The LBM is solved on a grid composed of cubic volumetric elements, and variable resolution is allowed, where the grid size changes by a factor of two for adjacent resolution regions. Figure 21 gives the resolution regions around the neck of the cavity and speakers. The finest region is located at the sharp edges of

the cavity neck and is 8 cells/mm in resolution. This resolution setting has been chosen based on mesh convergence tests on a similar geometry performed by the authors. In addition, the experimental ART is used to validate the simulation setup. In both the experimental and numerical ART the cavity probes are located in the center on the cavity floor.

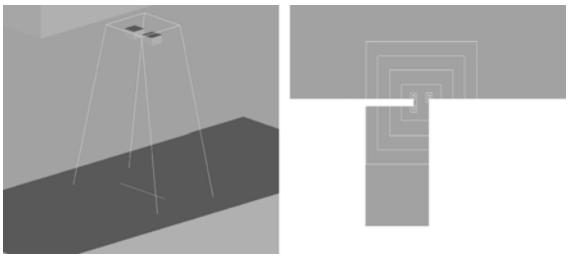

**Figure 21. Acoustic response test simulation setup. The resolution region boundaries are indicated by white contours. Across these boundaries the linear resolution is increased by a factor of two, with the finest region having 8 cells/mm. Two speakers, each with their own white noise signal are suspended 2 m above the cavity. Left figure gives 3d view of domain with speakers in top of figure and cavity slot below, right figure shows a vertical slice through cavity.**

Figure 22 shows the phases and magnitudes of the experimental and numerical ART. For both the experimental and numerical ART, the microphones are positioned at the quarter location in span, as indicated in figure 1. Table 5 shows the resonance frequency and quality factor of the complex transfer ratio fits. Due to the probe quarter location in the cavity some higher modes cannot be captured in this figure. The sound pressure level of the remaining higher mode around 1600 Hz is significantly lower and therefore not clearly distinguishable.

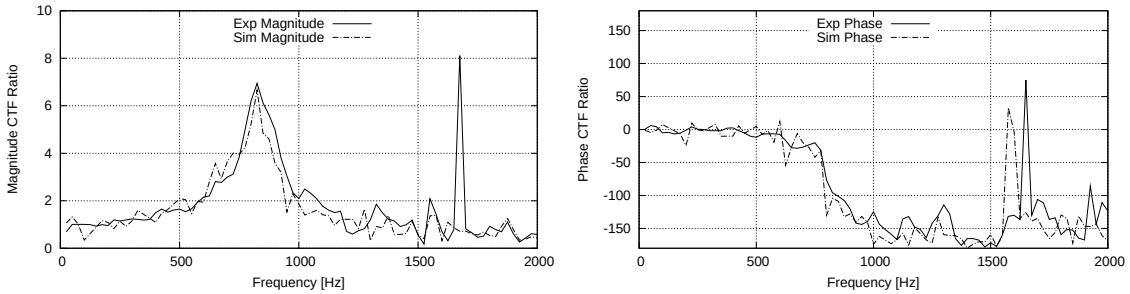


**Figure 22. Acoustic response test experiment and simulation results of the complex transfer function ratio magnitude(left) and phase (right).**

**Table 5. Experimental and simulation resonance frequency and quality factor.**

| | $f_H$ [Hz] | Q-factor |
|---|---|---|
| Simulation, sharp edges | 803 | 5.0 |
| Experiment, sharp edges | 828 | 5.9 |

According to table 5, the base resonance frequency is within 5 % of the experimental results. The acoustic non-compactness of the aperture causes high radiation losses, which accounts for the low observed Quality factors compared to compact aperture resonators.[30] The similarity between the experimental and numerical base resonance frequency and quality factor validate the use of an acoustic response test simulation to obtain the acoustic properties of slender cavities.

The acoustic simulation results are now used to investigate the observed behavior in experimental flow runs by band-filtering the pressure signal of the ART simulation. In this way maps of acoustic pressure intensity are obtained to check for the acoustic cavity behavior around the higher resonant modes.

Figure 23 shows the result of band-filtering the cavity pressure spectra around the most prominent modes observed in the experimental flow runs. This is displayed in a vertical plane through the resonator center. The used bandwidth is 25 Hz. The pressure maps correspond well to the pressure nodes and phase of the flow

experiment probes in figure 9. The shape of the modes can be viewed as the cavity subdividing itself into regions acting as separate Helmholtz resonators that interact with each other. The locations corresponding to the end masses of the Helmholtz resonators are then indicated in the figures by the low sound pressure regions and the locations of the Helmholtz resonator volumes themselves are indicated by the high sound pressure regions. In the next section an analytical model of the resonance frequency based on coupled Helmholtz resonators is derived based on these observations.

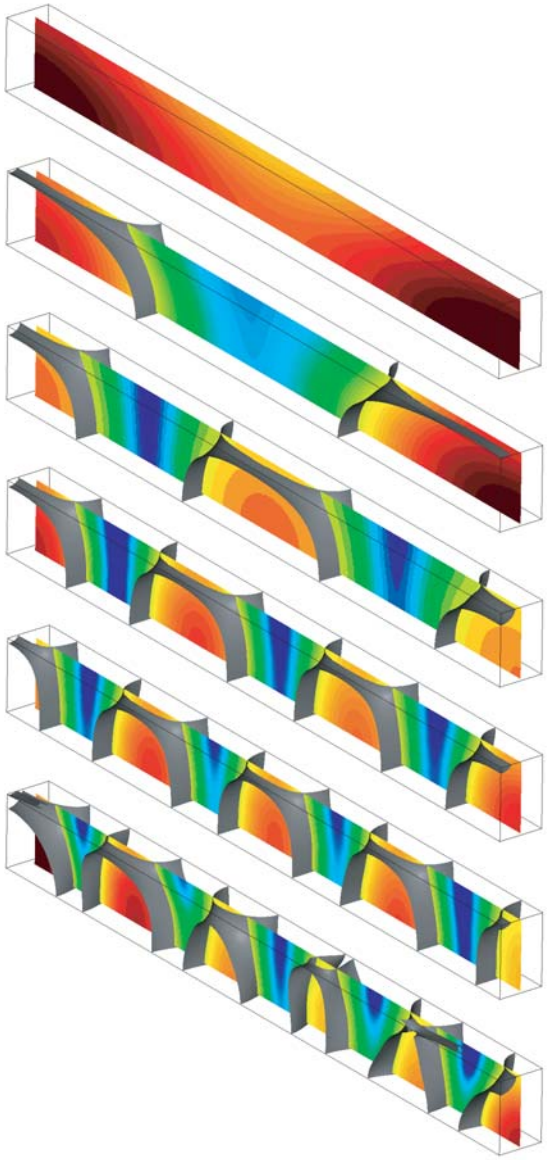

**Figure 23. (Color online) ART simulation band-filtered pressure signals in the cavity on a vertical plane through the cavity neck opening in dB for 825, 950, 1050, 1325, 1575 and 1925 Hz respectively. Level bandwidth is 20 dB, frequency bandwidth 25 Hz. 3d isosurfaces of constant sound pressure level are included. The cavity opening slot is located on top towards the viewer.**

## B. Analytical model spanwise modes

A lumped mass analytical model of the higher resonance modes is derived using the hypothesis that spanwise sections act as separate coupled Helmholtz resonators. In this section the resonance frequency of a system of $n$ spanwise resonators is determined and compared with the experimentally observed acoustic modes and simulation ART results.

The derivation of the lumped mass analytical model for the multiple Helmholtz resonator mode frequency is related to the derivation of the normal Helmholtz resonator frequency model. It is based on mass conservation in the resonator bodies and momentum conservation in the cavity openings and inter-resonator sections. The equations of a coupled system are explained in this section by using a setup of two spanwise resonators, see figure 24. In this figure $m$, $S$ indicate the masses and surface areas of the moving air columns, $V$ the volumes of the resonator sections and $W$ the widths of the inter-resonator and resonator sections. It is assumed that inter-resonator coupling occurs only within the cavity; acoustic coupling outside the cavity is neglected. Coherent compression is assumed within each resonator body.

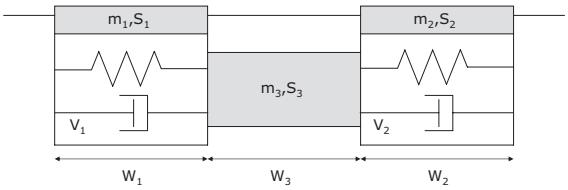


**Figure 24. Two coupled spanwise Helmholtz resonators.**

The integral mass conservation law applied to one resonator volume can be written as:

$$\frac{d}{dt}\int\int\int_V \rho dV = -\int\int_S \rho\vec{u}\cdot\vec{n}dS, \tag{13}$$

where $S$ is a control surface enclosing $V$ and $\vec{n}$ is the outer normal of $S$. Using a linear approximation and assuming uniform density $\rho$ and velocity $u$ and harmonic disturbances, Eq. (13) can be rewritten for the left and right resonator, respectively, as:

$$i\omega\frac{V_1}{c^2}p_1 = -\rho_0 u_1 S_1 - \rho_0 u_3 S_3 \tag{14}$$

$$i\omega\frac{V_2}{c^2}p_2 = -\rho_0 u_2 S_2 + \rho_0 u_3 S_3. \tag{15}$$

The only difference between a completely separate resonator and the coupled system is the right hand term $\rho_0 u_3 S_3$.

Application of the momentum law in a resonator neck opening yields in linear approximation:

$$\rho_0\frac{\partial u}{\partial t} = -\frac{\partial p}{\partial x}. \tag{16}$$

Assuming harmonic disturbances will give the following equations for the left and right resonator neck opening:

$$i\omega\rho_0 u_1 = \frac{p_1}{H_1'} \tag{17}$$

$$i\omega\rho_0 u_2 = \frac{p_2}{H_2'}. \tag{18}$$

Here $H' = H + h$ is the modified height of the oscillation mass in the cavity neck, as also used in Eq. (1). Application of the momentum law on the coupled mass in the center section yields:

$$i\omega\rho_0 u_3 = \frac{p_1 - p_2}{W_3}. \tag{19}$$

The two mass conservation Eqs. (14), (15) and the three momentum conservations Eqs. (17), (18) and (19) yield a matrix system to be solved. The geometric setup of the model of figure 24 depends on the width $W_3$ and area $S_3$ of the inter-resonator section and width of the resonator section $W_1$. The influence of these parameters on the frequency response is investigated by introducing the non-dimensionalized width $\alpha_1 = \frac{W_1}{W}$ and $\alpha_3 = \frac{W_3}{W}$, and non-dimensionalized effective area $\gamma = \frac{S_3}{A}$, where $A$ is the cross sectional area

of the cavity. The model is assumed to be geometrically symmetric so that $W_1 = W_2$, $V_1 = V_2$, $S_1 = S_2$ and $H_1' = H_2' = H'$. Solving the system for $f = \frac{\omega}{2\pi}$ yields an expression for the natural frequency:

$$f_2 = \frac{c}{2\pi}\sqrt{\frac{S}{VH'} + \frac{E}{W^2}}, \tag{20}$$

, where

$$E = \left(\frac{2\gamma}{\alpha_1\alpha_3}\right). \tag{21}$$

Compared to the resonance frequency of a single Helmholtz resonator (Eq. (1)) there is an additional term depending on the spanwise length $W$.

The natural resonance frequency for a system of arbitrary number of resonators in the cavity span $n = 1, 2, 3, ..$ can be found by organizing the the section width into a number of the dual resonator systems of Eq. 20 with reduced total span $\frac{W}{n-1}$. This will give:

$$f_n = \frac{c}{2\pi}\sqrt{\frac{S}{VH'} + \frac{E\left(n-1\right)^2}{W^2}}. \tag{22}$$

For $n = 1$, Eq. 1 is retrieved.

Using spanwise integration of the ART results bandfiltered cavity volume shown in figure 23, the magnitudes of $\alpha_1, \alpha_2$ can be estimated. This will give $\alpha_1 \approx \frac{1}{\pi}, \alpha_3 \approx \frac{2}{\pi}$. Note that due to the gradual change in span, the widths of the inter-resonator and resonator sections do not add up to the total spanwise width exactly, but partly overlap. Filling in will give:

$$f_n = \frac{c}{2\pi}\sqrt{\frac{S}{VL'} + \beta\left(\frac{\pi\left(n-1\right)}{W}\right)^2}, \tag{23}$$

with $\beta$ of order 1, accounting for variations in resonator effective cross-section and widths. The used lumped mass model derivation indicates that $n$ interacting Helmholtz resonators are present in the span. It should be noted however that equation 23 can also be interpreted as combination of Helmholtz resonance and spanwise planar wave modes.

The derived analytical model for multiple Helmholtz resonators of Eqs. 23 is compared with the experimental flow run results in table 6. When $\beta = 0.97$ is chosen, a good match with the experimentally obtained modes can be found. Table 6 includes flow run data from the 0.3 m and 0.5 m span cavity flow run experiments. The base Helmholtz resonance effective length $H'$ is set to match the base resonance frequency. The analytical resonance frequencies are all within a few percent of the observed experimental values. This result is obtained by using only one chosen variable $\beta$ and thus the analytical model seems to be able to describe the observed physical behavior.

**Table 6. Comparison analytical model multiple Helmholtz resonators with flow run higher mode frequencies, $\beta = 0.97$. Large (0.5 m) and small (0.3 m) span flow experiments included.**

| large span (0.5 m) nr. of sections | analytical freq. [Hz] | exp. freq. [Hz] (flow-run based) |
|---|---|---|
| 1 | 830 | 830 (set) |
| 2 | 897 | 900 |
| 3 | 1074 | 1050 |
| 4 | 1318 | 1300 |
| 5 | 1597 | 1600 |
| 6 | 1897 | 1900 |
| small span (0.3 m) nr. of sections | analytical freq. [Hz] | exp. freq. [Hz] (flow-run based) |
| 1 | 830 | 830 (set) |
| 2 | 1006 | 1000 |
| 3 | 1408 | 1420 |



## VIII. Cavity flow simulations

In this section the CFD flow simulations of the cavity base resonance mode are presented. The reasons for performing flow simulations are two-fold. First of all it is used to investigate the effect of inflow conditions on the resonance behavior. Secondly it is implemented to investigate the ability of the Lattice Boltzmann method to simulate these resonance phenomena and under what conditions. The simulations are conducted using a research version of PowerFLOW.

### A. Steady inlet simulations

First steady inlet simulations are performed with the $K - \epsilon$ turbulence model turned on and also with the $K - \epsilon$ turbulence model off. I this last case the solver behaves as an implicit large eddy simulation (ILES). A wall model is included in both cases. The cavity with has been set to 10 times the streamwise opening length $\delta$ of 8 mm. The resolution setup is given in figure 25, where the regions around the opening edges have the finest resolution of 16 cells/mm. The rest of the cavity opening has a resolution of 8 cells/mm and the lower boundary layer has a resolution of 2 cells/mm.

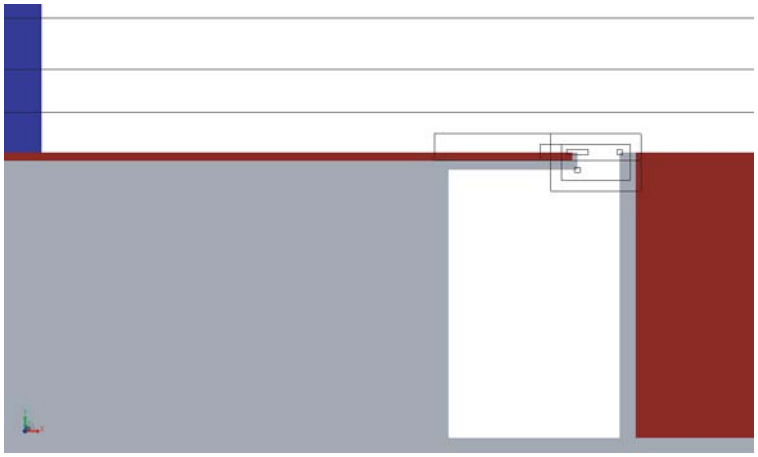

**Figure 25. Side view of flow simulation setup. The variable resolution regions are shown by outline, with the highest resolution of 16 cells/mm at cavity opening edges.**

Several flow velocities in the range 20-30 m/s have been simulated. Figure 26 shows the pressure time series of the cavity internal probe for the most resonating flow velocity, 24 m/s.

The simulation with $K-\epsilon$ turbulence model on shows no resonance, fluctuations diminish. This is expected due to the fact that the Reynolds number based on the cavity opening $Re \approx 10^4$ is too low to be modeled with the turbulence model.

The ILES results show a higher resonance amplitude compared to experiments, which could be attributed to the lack of turbulent fluctuations. It is expected for the boundary layer turbulence to disrupt the coherency of the shear layer thus to reduce resonance amplitude compared to a boundary layer of similar shape without fluctuations. To test this hypothesis transient inlet seeding has been implemented in the next sections.

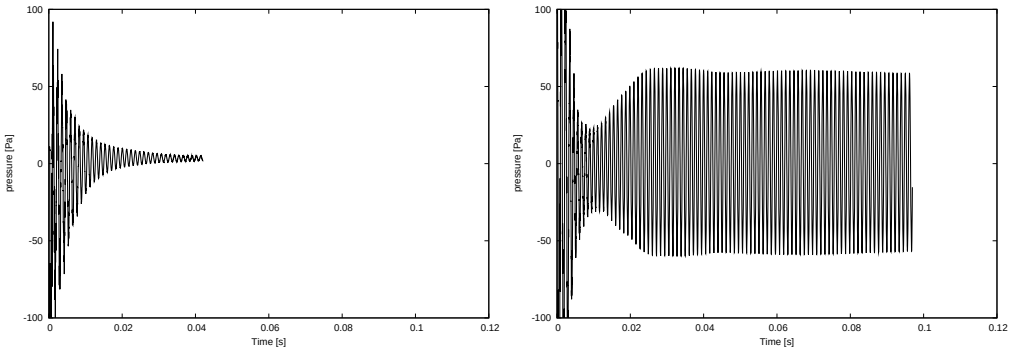


(a) $K-\epsilon$ model, 24 m/s (b) ILES, 24 m/s

**Figure 26. Pressure time series of cavity internal pressure for steady inlet simulations.**

## B. Flat plate boundary layer simulations

In order to implement transient inlet seeding into the cavity domain, fluctuations need to be produced that resemble the turbulent structures in the boundary layer. For this, a flat plate boundary layer has been simulated where the flow is perturbed by a zigzag type turbulator strip.

The simulation setup for generation of the direct fluctuations consists of a flat plate with a turbulator strip geometry of which a section is shown in figure 27. The simulation domain is big enough to allow boundary layer development similar to the experiments. The boundary layer properties are measured 0.2 to 0.7 m after the turbulator, similar to experiments. The turbulator strip has the same similar dimensions as in experiment; 1 mm thickness, 10 mm streamwise length and 9 mm spanwise repetition of the teeth. The width of the domain is smaller than experiment (80 mm wide instead of 600 mm) in order to prevent the simulation from becoming too computationally expensive. The resolution in the lower region of the boundary layer is 2 voxels/mm and around the strip 8 voxels/mm.

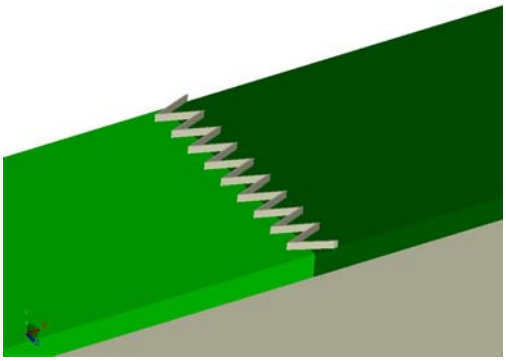

**Figure 27. Turbulator strip simulation setup**

Figures 28 shows the mean and RMS profiles of ILES simulations compared with hotwire experiments. A $K-\epsilon$ model simulation without a turbulator strip has been included for comparison. The mean and RMS profiles of the turbulator strip simulations closely resemble the experimental results. The simulation without a turbulator has practically no direct fluctuations, only modeled eddy viscosity.

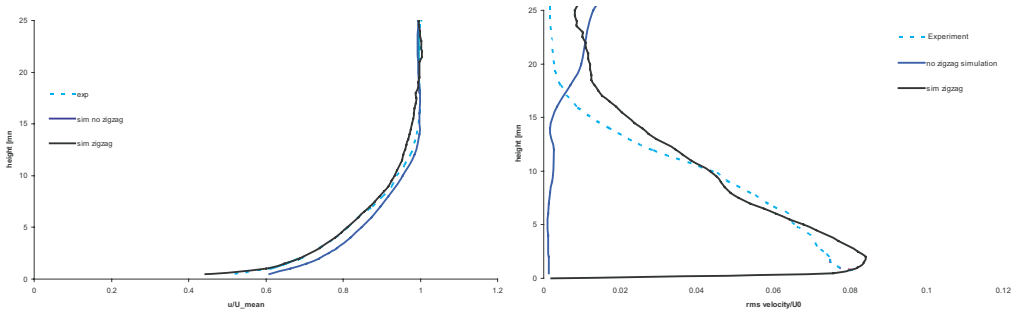


(a) mean (b) rms

**Figure 28. Turbulator strip simulation boundary layer mean and rms velocity profiles, 24 m/s free stream velocity. ILES simulation with strip indicated in solid black, $K-\epsilon$ model simulation without strip indicated in solid blue. The dotted lines are experimental results.**

Figure 29 shows the spectrum of the simulated fluctuations and compares them with experimental results. The power spectral density of pressure has been used. The dimensionless streamwise velocity magnitudes are used for the comparison. Simulation fluctuations are comparable to the experiments for until a cutoff around 5 kHz.

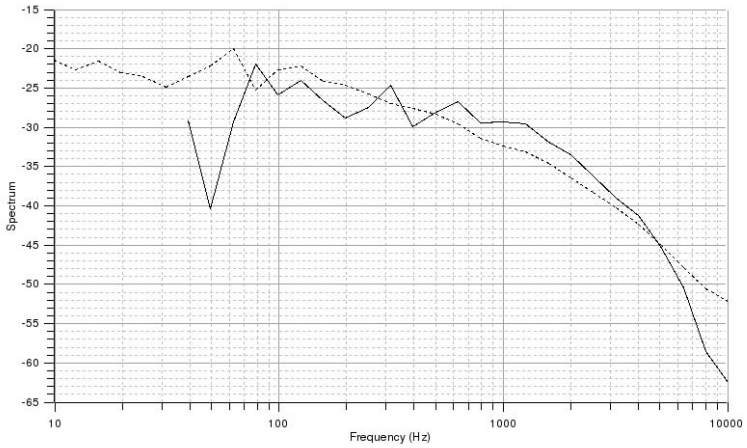


**Figure 29. Streamwise velocity power spectral densities at 3 mm height in the boundary layer. Experiment is indicated with dotted line.**

The turbulent vortices in the boundary layer are visualized by isosurfaces of the Lambda2 criterion for vortex detection in figure 30. Lambda2 is the second largest eigenvalue of $S^2+\Omega^2$ , with S the symmetric deformation tensor and $\Omega$ the anti-symmetric spin tensor. One can see that the ordered wake structures of the turbulator strip decay into turbulent vortices that are convected downstream.

## C. Unsteady inlet simulations using inlet seeding

The fluctuation content ( all 3 velocity components u, v, w, density $\rho$ and pressure p ) in the flat plate boundary layer is recorded at 40 kHz and seeded into the inlet of the cavity simulations. The the unsteady inlet conditions are implemented in ILES cavity simulations. Again several flow velocities in the range 20-30 m/s have been evaluated and the most resonating case of 24 m/s is plotted. Figure 31 shows the pressure time series of the cavity internal probe, with experimental results included for comparison. The CFD average amplitude of resonance is resembling the experimental results. However, there seems to be more resonance intermittency in the CFD time signal. This can potentially be due to the limited spanwise width or due to an overprediction of the large scale boundary layer fluctuations. On overall, cavity resonance features can be simulated using the current methodology.

Figure 32 shows the spanwise vorticity in the opening of the cavity. Experimental results are included.

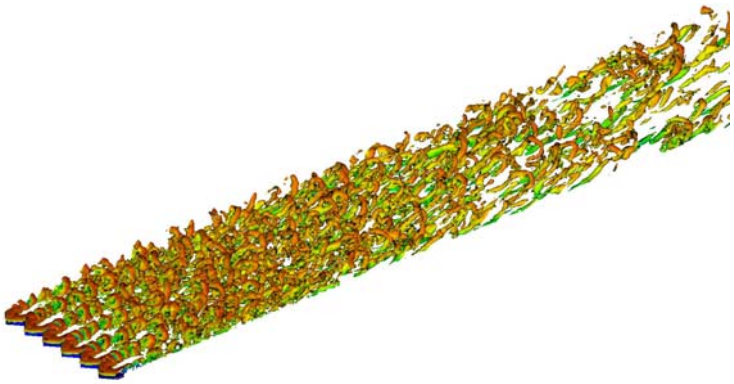

**Figure 30. Iso-surfaces of Lambda2 criterion colored by velocity magnitude for part of the strip simulation.**

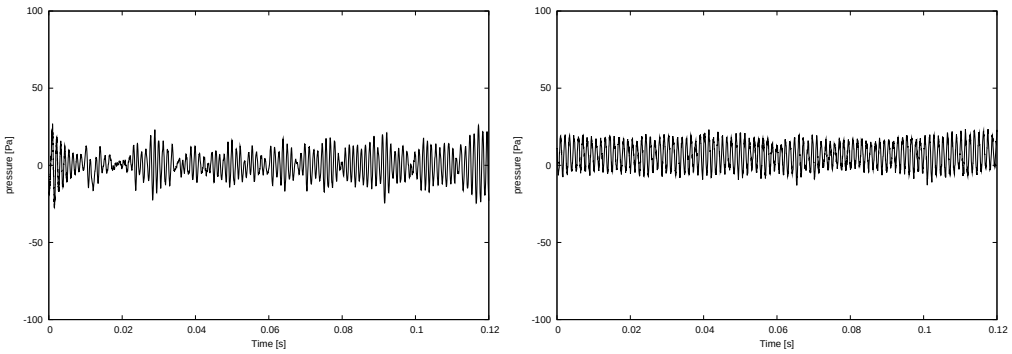


(a) CFD, ILES, unsteady inlet, 24 m/s (b) experiment, 24 m/s

**Figure 31. Pressure time series of cavity internal pressure for experimental and unsteady inlet simulation.**

The results show interaction of boundary layer fluctuations with the shear layer that can explain the intermittency in the cavity pressure time series due to disruption of the coherency of the shear layer. The simulations confirm the reduction of resonance amplitude due to turbulent fluctuations.

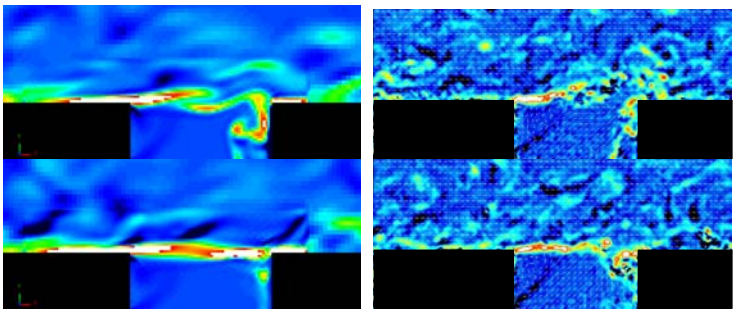

**Figure 32. Two time instances of spanwise vorticity for unsteady inlet CFD simulations (left) and experiment (right). Color range -5000 - 30000 1/s.**

## IX. Conclusions

An experimental and numerical study on simplified door gap geometries has been conducted. With increasing velocity, several modes can be observed. The experimental study included high speed PIV vizualization of the flow around the cavity opening. The numerical investigation is performed using a Lattice Boltzmann based code.

For investigation he base mode without spanwise variations the upstream and downstream opening sections have been varied, as well as the lip overhang location and boundary layer thickness. Increase in boundary layer thickness reduces the resonance amplitude. Only upstream lip overhang cases show resonance lock-on. Flow visualization show a large trapped vortex for the downstream overhang cases, reducing the effective shear and causing a cavity internal flow component of 0.1 U. This can explain the lack of resonance in the downstream overhang geometries. Rounding of the downstream edges reduces the resonance amplitude. Investigation of the flow field shows that in this case the stagnation point on the downstream wall is lowered, indicating less flow entrapment into the cavity for a given shear layer deflection. Rounding of the upstream edges increases resonance. Evaluation of the shear layer fluctuations indicates that in this case the first section of the shear layer exhibits more fluctuations and the effective length of the shear layer is increased. Both effects increase the maximum deflection of the shear layer at the downstream edge and thus promote resonance.

The geometry with a upstream edge overhang and sharp edges shows a number of higher modes present with spanwise variations. An acoustic response test in absence of flow is simulated and compared with experimental results. The comparison confirms that LBM based simulations are able to simulate the cavity acoustic response. Pressure band filtering of the simulation pressures reveals mode shapes of the higher modes observed in flow experiments. An analytical model for the resonance frequencies is derived that resembles the observed frequencies well.

The geometry with a upstream edge overhang and sharp edges is simulated using the Lattice Boltzmann method. Simulations with steady inflow conditions show an overprediction of resonance. A flat plate simulation with zigzag type turbulator strip has been implemented to create turbulent fluctuations. The mean, RMS profiles and velocity spectra resemble experimental hotwire results well. The fluctuations are implemented in a cavity simulation. The resonance amplitude matches experiment, but there is an increased intermittency of resonance amplitude in time. Comparison with PIV shows a similar influence of turbulent fluctuations on the shear layer, confirming the reducing effect of fluctuations on resonance amplitude. The flow simulations indicate that the LBM with the current setup is able to simulate door gap cavity resonance.

## Acknowledgments

We would like to thank Prof. Hirschberg from Eindhoven University of Technology for the helpful advice on cavity acoustics and advice on design of the experimental setup. We also would like to thank Stefan Bernardi at the Delft university of Technology low speed laboratory for helping setting up the wind tunnel experiments. From Exa Corp. we would like to thank Dr. Bernd Crouse and Dr. David Freed for the support. At the aerodynamics department of Delft University we would like to thank Dr. Leo Veldhuis for his helpful discussions and Prof. Fulvio Scarano for his experimental expertise.

## References

[1]J. E. Rossiter, *Wind-tunnel experiments on the flow over rectangular cavities at subsonic and transonic speeds*, 1st edition (London, H.M.S.O.) (1967).

[2]P. Radavich, A. Selamet, and J. Novak, "A computational approach for flow-acoustic coupling in closed side branches", J. Acoust. Soc. Am. **109**, 1343–1353 (2001).

[3]S. Dequand, S. Hulshoff, and A. Hirschberg, "Self-sustained oscillations in a closed side branch system", J. Sound Vib. **265**, 359–386 (2003).

[4]S. Dequand, X. Luo, J. Willems, and A. Hirschberg, "Helmholtz-like resonator self-sustained oscillations, part 1: Acoustical measurements and analytical models", AIAA **41**, 408–415 (2003).

[5]S. Dequand, S. Hulshoff, H. Kuijk van, J. Willems, and A. Hirschberg, "Helmholtz-like resonator self-sustained oscillations, part 2: Detailed flow measurements and numerical simulations", AIAA **41**, 416–424 (2003).

[6]S. Dequand, J. F. H. Willems, M. Leroux, R. Vullings, M. van Weert, C. Thieulot, and A. Hirschberg, "Simplified models of flue instruments: Influence of mouth geometry on the sound source", J. Acoust. Soc. Am. **113**, 1724–1735 (2003).

[7]J. Coltman, "Jet drive mechanism in edge tones and organ pipes", J. Acoust. Soc. Am. **60**, 725–733 (1976).

[8]S. A. Elder, "On the mechanism of sound production in organ pipes", J. Acoust. Soc. Am. **54**, 1554–1564 (1973).

[9]B. Crouse, S. Senthooran, G. Balasubramanian, D. Freed, S. Noelting, L. Mongeau, and J. Hong, "Sunroof buffeting of a simplified car model: Simulations of the acoustic and flow-induced responses", 2005-01-2498 (2005).

[10]D. Ricot, V. Maillard, and C. Bailly, "Numerical simulation of the unsteady flow past a cavity and application to sunroof buffeting", in *7th AIAA/CEAS Aeroacoustics Conference* (Maastricht, The Netherlands) (2001).

[11]U. Ingard, "On the theory and design of acoustic resonators", J. Acoust. Soc. Am. **25**, 1037–1061 (1953).

[12]M. Howe, "Low strouhal number instabilities of flow over apertures and wall cavities", J. Acoust. Soc. Am. **102**, 772–780 (1997).

[13]G. Kooijman, A. Hirschberg, and J. Golliard, "Acoustical response of orifices under grazing flow: Effect of boundary layer profile and edge geometry", J. Sound Vib. **315**, 849–874 (2008).

[14]P. A. Nelson, N. A. Halliwell, and P. E. Doak, "Fluid dynamics of a flow excited resonance, part i: Experiment", J. Sound Vib. **78**, 15–38 (1981).

[15]P. A. Nelson, N. A. Halliwell, and P. E. Doak, "Fluid dynamics of a flow excited resonance, part ii: Flow acoustic interaction", Journal of Sound and Vibration **91**, 375–402 (1983).

[16]B. S. Henderson, "Category 6 automobile noise involving feedback - sound generated by low speed cavity tones", NASA Tech. Rep. (2000).

[17]B. S. Henderson, "Category 5: Sound generation in viscous problems, problem 2: Sound generation by flow over a cavity", NASA Tech. Rep. (2004).

[18]L. Mongeau, J. D. Bezemek, and R. Danforth, "Pressure fluctuations in a flow-excited door gap model", SAE (1997).

[19]L. Larchevêque, P. Sagaut, T. H. Lê, and P. Comte, "Large-eddy simulation of a compressible flow in a three dimensional open cavity at high reynolds number", J. Fluid Mech. 265–301 (2004).

[20]S. Elder, T. Farabee, and F. DeMetz, "Mechanisms of flow-excited cavity tones at low mach number", J. Acoust. Soc. Am. **72**, 532–549 (1982).

[21]X. Gloerfelt, "Cavity noise", `http://sin-web.paris.ensam.fr/squelettes/ref_biblio/Gloerfelt_VKI_2009a.pdf` (date last viewed 10/26/09) (2009).

[22]S. Succi, *The lattice Boltzmann equation for fluid dynamics and beyond* (Oxford University Press, Oxford) (2001).

[23]P. L. Bhatnagar, E. P. Gross, and M. Krook, "A model for collision processes in gases. i. small amplitude processes in charged and neutral one-component systems", Phys. Rev. **94**, 511–525 (1954).

[24]G. Chen, S. andDoolen, "Lattice boltzmann method for fluid flows", Ann. Rev. Fluid Mech. **30**, pp 329–364 (1998).

[25]B. Crouse, D. M. Freed, G. Balasubramanian, S. Senthooran, P. Lew, and L. Mongeau, "Fundamental aeroacoustic capabilities of the lattice-boltzmann method", 2006-2571 (AIAA conference, Cambridge, Massachussets) (2006).

[26]D. M. Freed, "Powerflow for acoustics simulations", (Exa Corp., Tokio, Japan) (2006).

[27]A. A. da Silva and G. Scavone, "Lattice boltzmann simulations of the acoustic radiation from waveguides", Journal of Physics A **40**, 397–408 (2007).

[28]X. M. Li, R. C. Leung, and R. M. C. So, "One-step aeroacoustics simulation using lattice boltzmann method", AIAA Journal **44**, 78–89 (2006).

[29]F. M. White, *Viscous Fluid Flow*, 2 edition (McGraw-Hill, New York) (1991).

[30]A. Hirschberg and S. W. Rienstra, "An introduction to aeroacoustics", `http://www.win.tue.nl/~sjoerdr/papers/les-swr-mh.pdf` (date last viewed 10/26/09) (2004).